K. E. N'souglo, A. Srivastava, S. Osovski, J. A. Rodríguez-Martínez. Random distributions of initial porosity trigger regular necking patterns at high strain rates, in: *Proceedings of the Royal Society A: mathematical, physical and engineering sciences*, 474, (2211), 20170575, March 2018

DOI: https://doi.org/10.1098/rspa.2017.0575

Random distributions of initial porosity trigger regular necking patterns at high strain rates

K. E. N'souglo[1], A. Srivastava[2], S. Osovski[3] and J. A. Rodríguez-Martínez[1]

[1]Department of Continuum Mechanics and Structural Analysis. University Carlos III of Madrid, Leganés, Madrid, Spain

[2]Department of Materials Science and Engineering, Texas A&M University, College Station, TX, USA

[3]Faculty of Mechanical Engineering, Technion - Israel Institute of Technology, Haifa, Israel

At high strain rates the fragmentation of expanding structures of ductile materials in general starts by the localization of plastic deformation in multiple necks. Two distinct mechanisms have been proposed to explain multiple necking and fragmentation process in ductile materials. One view is that the necking pattern is related to the distribution of material properties and defects. The second view is that it is due to the activation of specific instability modes of the structure. Following this, we investigate the emergence of necking patterns in porous ductile bars subjected to dynamic stretching at strain rates varying from $10^3\ s^{-1}$ to $0.5 \cdot 10^5\ s^{-1}$ using finite element calculations and linear stability analysis. In the calculations the initial porosity (representative of the material defects) varies randomly along the bar. The computations revealed that, while the random distribution of initial porosity triggers the necking pattern, it barely affects the average neck spacing, especially, at higher strain rates. The average neck spacings obtained from the calculations are in close agreement with the predictions of the linear stability analysis. Our results also reveal that the necking pattern does not begin when the Considère condition is reached but is significantly delayed due to the stabilizing effect of inertia.

1. Introduction

The first mechanism behind the fragmentation of expanding structures of ductile materials at high loading rates was proposed nearly 70 years ago by N. F. Mott. With world war II as backdrop, Mott theoretically described the process of fragmentation resulting from the explosive rupture of cylindrical structures. Mott's ideas on fragmentation were embodied in several classified reports for the Ministry of Supply of the United Kingdom between January and May of 1943 [1–4]. In Mott's words, in this series of works *a tentative theory was given to account for the mean fragment sizes of certain types of bomb and shell, and for the relative numbers of large and small fragments*. Between August of 1943 and December of 1944, Mott issued additional classified reports that provided a re-examination of the available experimental data on the break-up of shell and bomb casings based on his proposed mechanism and theory [5,6]. The first open publication which collected the core of Mott's theory of fragmentation came to light in 1947 in the Proceedings of the Royal Society [7].

Mott's theory of fragmentation is essentially a statistical one-dimensional model that considers the onset of fractures as random processes which respond to the inherent variability in the strain to fracture of ductile materials. To support this assumption, he relied on experimental observations of fracture in notched-bar specimens (tested quasi-statically) which showed that the reduction in the cross-sectional area of different specimens of the same material, varied from specimen to specimen. In particular, Mott discussed the scatter of $\pm 1\%$ in the reduction in area of notched steel specimens at fracture. Mott proposed that the statistical nature of the fracture process, i.e. the scatter in the strain to fracture, determined both the characteristic fragment size, as well as the distribution in fragment sizes. He postulated that *fracture begins, as in brittle materials, at one of a number of "weak points" distributed throughout the material*. While he stated that his theory was applicable only to casings which expand plastically before rupture, he did not consider explicitly the plastic localization patterns that usually appear in ductile materials prior to fracture. He, however, stated that the fracture energy was not significant and fractures were assumed to occur instantaneously. Following Mott's theory of fragmentation, when instantaneous fracture occurs at one point, stress waves (or the Mott's waves) propagate away from the fracture releasing the stress in the neighborhood. The unstressed regions spread with a velocity that depends on the material density, the strain rate and the yield stress at failure. Within the regions of the specimen subjected to the action of the release waves the material does not continue to stretch and thus failure is precluded. The size of the fragments is then determined by the distance traveled by the Mott's wave. A more complete and detailed chronological description of the work of Mott can be found in the book by Grady [8].

Over the past three decades, Grady and co-workers further popularized Mott's theory of fragmentation. In a series of papers, Grady and collaborators [9–11] modified and enriched the original theory of Mott to account for the dissipation of energy associated with the fracture process. Grady argued that *some degree of work must be expended, and some fracture energy overcome, in opening the cracks delineating the fragment boundaries produced in the fragmentation event* [8]. This extended the stress release analysis developed by Mott to calculate the time history of plastic release waves emanating from sites of fracture, and thus the average fragment size. Nevertheless, the specific deformation mechanisms (e.g. necking, shear banding etc.) prior to fragmentation that lead to dissipation and fracture growth were only addressed tangentially. The authors did, however, acknowledge the influence of such deformation mechanisms on the fragmentation characteristics. The works [12–14], made apparent that the fragmentation characteristics and the distribution of fragment size depends on the specific localization mechanism and pattern that develops before final fracture.

More recently, Zhang and Ravi-Chandar [12–14] performed a series of experiments using aluminum and copper rings and cylinders expanded radially at strain rates ranging from $5 \cdot 10^3\ s^{-1}$ to $1.5 \cdot 10^4\ s^{-1}$. The nominal wall thickness of the specimens in these experiments was $0.5\ mm$. For all the tests performed, several fractures occurred in the specimens, that

were preceded by the development of multiple necks. The authors carefully measured the distance between the necks and the number of fragments. In all the cases, the number of necks were greater than the number of fracture sites. The experimental results were interpreted using Mott's theory, which allowed the authors to conclude that the number of necks are dictated by statistical distribution of material property and local microstructure. They also stated that, in all the experiments, the necks nucleated at the Considère strain, independent of the applied loading rate, at least, for the materials investigated. With the aim of explaining these experimental observations, Ravi-Chandar and Triantafyllidis [15] developed a 1D numerical model to analyze the time-dependent response to strain perturbations of ductile bars subjected to dynamic stretching. The mechanical behavior of the bar was described using a nonlinear elastic constitutive law. The authors tracked the evolution of the strain perturbations during the loading process and showed that the perturbations travel along the bar, at a speed that decreases with strain, until the Considère strain is reached, thereafter the perturbations are arrested at specific locations in the specimen. These locations were assumed to control the positions where the necks nucleate, leading to multiple necking and fragmentation observed in the experiments. Furthermore, Dequiedt [16] suggested that the potential sites of fracture, instead of being determined by a random distribution of point defects as in the classical fragmentation analyses, could be linked to zones of strain concentration that develop due to the activation of specific instability modes (e.g. necking) in the specimen/structure.

The existence of unstable modes that determine the localization patterns preceding the fragmentation of ductile materials was originally suggested by Molinari and co-workers [17–22] and Freund and co-workers [23,24], and later by others [25–27]. Using linear stability analysis, in which a small perturbation is added to the fundamental solution of the problem, previous authors determined the loading conditions and material behaviors for which a neck-like deformation field can develop in problems representative of axially-symmetric structures (e.g. rings, tubes, hemispheres) subjected to dynamic expansion. The existence of growing instability modes was shown to be a result of the combined effects of inertia, stress state and constitutive behavior of the material. The mode that grows the fastest, at each time, is referred to as the critical mode, and it is assumed to dictate the average neck spacing in the multiple localization pattern. In such a sense, the linear stability analyses approach argues for the inclusion of a deterministic component to the mechanism behind multiple necking and fragmentation process.

In summary, the past efforts to address multiple necking (or strain localization) and fragmentation process has led to two proposed mechanisms: (i) The localization and fracture sites at high strain rates are related to the statistical distribution of material property and microstructural heterogeneities; (ii) The localization and fracture sites are determined by the activation of specific instability modes in the structure rather than the random distribution of defects. Following this, we have carried out 3D finite element calculations of porous ductile cylindrical bars subjected to dynamic stretching. In the bars the initial porosity (representative of initial material defects) varies statistically along the bar and the mechanical behavior of the porous ductile material is described using an elastic-viscoplastic constitutive relation for a progressively cavitating ductile solid. The numerical calculations mimic the experiments that form the basis of the first proposed mechanism of multiple necking and fragmentation. In addition, we have developed linear stability analysis for porous ductile materials following the ideas of Molinari and co-workers [17–22], and Freund and co-workers [23,24] that form the basis of second proposed mechanism of multiple necking and fragmentation. To the best of authors' knowledge, the linear stability analysis for porous ductile material based on elastic-viscoplastic constitutive relation for a progressively cavitating solid has not been attempted before.

The results presented in this paper, show a good agreement between the predictions of analytical model (linear stability analysis) and 3D finite element calculations for applied strain rates ranging from $10^3\ s^{-1}$ to $0.5 \cdot 10^5\ s^{-1}$. The agreement between the predictions of the analytical model and numerical calculations over two decades of applied strain rate provides a complete understanding of the multiple necking process. For example, we show that while

the statistical distribution of initial porosity (statistical distribution of material defects) acts as a trigger for the localization of plastic deformation, it barely affects the average neck spacing of the localization pattern that emerges in the bar at large strains, especially, for the higher strain rates investigated. The results presented here also reveal that the (full) localization pattern does not begin when the Considère condition is reached. On the contrary, due to the stabilizing effect of inertia, the formation of the final necking pattern is delayed until the strain level in the bar reaches values that, for the strain rates considered, can be several times greater than the Considère strain. We also compare our results (both analytical and numerical) with the numerical simulations reported by Guduru and Freund [28] for smooth bars of aluminum and copper with homogeneous distribution of the initial porosity (instead of varying statistically). In [28] the localization was triggered by the numerical perturbations introduced by the finite element code, nevertheless, a good qualitative agreement between their results and ours, in terms of localization strain and average neck spacing, has been found for a wide range of strain rates.

An outline of the paper is as follows. In section 2, we describe the basic equations of the elastic-viscoplastic constitutive model for progressively cavitating solid used to describe the mechanical behavior of the porous ductile materials. Sections 3 and 4 show, respectively, the analytical and numerical models developed to calculate the average neck spacing of the multiple localization patterns that develop in cylindrical bars subjected to dynamic stretching. Section 5 presents the numerical results which are then compared with the analytical predictions in section 6. Finally, section 7 provides a brief summary of the paper and the main conclusions derived from this work.

2. Constitutive framework

The constitutive framework used to model the dynamic response of porous cylindrical bars is the modified Gurson constitutive relation [29–32] with the flow potential having the form:

$$\Phi\left(\Sigma_h, \Sigma_e, \bar{\sigma}, f^*\right) = \left(\frac{\Sigma_e}{\bar{\sigma}}\right)^2 + 2q_1 f^* \cosh\left(\frac{3q_2\Sigma_h}{2\bar{\sigma}}\right) - 1 - \left(q_1 f^*\right)^2 \tag{2.1}$$

where f^* is the effective porosity (see Eq. (2.10)), q_1 and q_2 are material parameters, and $\bar{\sigma}$ is the matrix flow strength given as:

$$\bar{\sigma} = \Psi\left(\bar{\varepsilon}^p, \dot{\bar{\varepsilon}}^p, T\right) = \sigma_0 \left(1 + \frac{\bar{\varepsilon}^p}{\varepsilon_0}\right)^n \left(\frac{\dot{\bar{\varepsilon}}^p}{\dot{\varepsilon}_0}\right)^m G(T) \tag{2.2}$$

with, $\bar{\varepsilon}^p = \int_0^t \dot{\bar{\varepsilon}}^p(\tau)d\tau$, where $\dot{\bar{\varepsilon}}^p$ is the effective plastic strain rate in the matrix material, σ_0 is the reference yield stress, n is the strain hardening exponent, m is the rate sensitivity exponent, ε_0 is the reference strain, and $\dot{\varepsilon}_0$ is the reference strain rate. The temperature-dependence of the matrix flow strength is given by:

$$G(T) = 1 + b\exp\left(-c\left[T_0 - 273\right]\right)\left\{\exp\left(-c\left[T - T_0\right]\right) - 1\right\} \tag{2.3}$$

where, b and c are material parameters, and T_0 is the reference temperature. In Eq. (2.1), Σ_h and Σ_e are the macroscopic hydrostatic and effective stresses given as:

$$\Sigma_h = \frac{1}{3}\boldsymbol{\Sigma} : \mathbf{1}; \qquad \Sigma_e = \sqrt{\frac{3}{2}\boldsymbol{\Sigma}'\boldsymbol{\Sigma}'}; \qquad \boldsymbol{\Sigma}' = \boldsymbol{\Sigma} - \Sigma_h : \mathbf{1} \tag{2.4}$$

In Eq. (2.4), $\boldsymbol{\Sigma}$ is the macroscopic Cauchy stress tensor and $\mathbf{1}$ is the unit second order tensor. The macroscopic rate of deformation tensor $\dot{\mathbf{E}}$ is decomposed as the sum of an elastic $\dot{\mathbf{E}}^e$ and a plastic part $\dot{\mathbf{E}}^p$:

$$\dot{\mathbf{E}} = \dot{\mathbf{E}}^e + \dot{\mathbf{E}}^p \tag{2.5}$$

The relation between the macroscopic elastic strain rate and the macroscopic stress rate is given by the following hypo-elastic law:

$$\hat{\boldsymbol{\Sigma}} = \mathbf{C} : \dot{\mathbf{E}}^e \tag{2.6}$$

where $\hat{\boldsymbol{\Sigma}}$ is the Jaumann rate of Cauchy stress and $\mathbf{C}$ is the tensor of isotropic elastic moduli given by:

$$\mathbf{C} = 2G\mathbf{I}' + K\mathbf{1} \otimes \mathbf{1} \tag{2.7}$$

with G being the elastic shear modulus, K being the bulk modulus and $\mathbf{I}'$ the unit deviatoric fourth order tensor.

Assuming that the rate of macroscopic plastic work is equal to the rate of equivalent plastic work in the matrix material, it follows that:

$$\boldsymbol{\Sigma} : \dot{\mathbf{E}}^p = (1 - f)\, \bar{\sigma} \dot{\bar{\varepsilon}}^p \tag{2.8}$$

where f is the void volume fraction.

The plastic part of the rate of macroscopic deformation follows the direction normal to the flow potential:

$$\dot{\mathbf{E}}^p = \dot{\lambda} \frac{\partial \Phi}{\partial \boldsymbol{\Sigma}} \tag{2.9}$$

where $\dot{\lambda}$ is the plastic flow proportionality factor. The function f^* introduced in [32] is given by:

$$f^* = \begin{cases} f & \text{if} \quad f < f_c \\ f_c + \dfrac{(f_u - f_c)\,(f - f_c)}{(f_f - f_c)} & \text{if} \quad f_c \leqslant f \leqslant f_f \\ f_u & \text{if} \quad f > f_u \end{cases} \tag{2.10}$$

where f_c is the void volume fraction at which voids coalesce, f_f is the void volume fraction at fracture of the material and $f_u = 1/q_1$ is the ultimate void volume fraction.

The initial void volume fraction is f_0 and, assuming the incompressibility of the matrix material, the evolution of the void volume fraction is defined as:

$$\dot{f} = (1 - f)\, \dot{\mathbf{E}}^p : \mathbf{1} \tag{2.11}$$

Assuming adiabatic conditions of deformation (no heat flux) and considering that plastic work is the only source of heating, we get:

$$\rho C_p \frac{\partial T}{\partial t} = \beta \boldsymbol{\Sigma} : \dot{\mathbf{E}}^p \tag{2.12}$$

with ρ being the current density, C_p the specific heat and β the Quinney-Taylor coefficient. According to the principle of mass conservation, the current density is:

$$\rho = \frac{\rho_0}{\det(\mathbf{F})} \tag{2.13}$$

where ρ_0 is the initial density and $\mathbf{F}$ is the deformation gradient tensor.

The above formulation is complemented with the loading/unloading Kuhn-Tucker conditions:

$$\dot{\lambda} \geqslant 0; \qquad \Phi \leqslant 0; \qquad \dot{\lambda}\Phi = 0 \tag{2.14}$$

and the consistency condition during plastic loading:

$$\dot{\Phi} = 0 \tag{2.15}$$

Table 1 shows the parameters used in the stability analysis and the finite element calculations. Similar set of parameters were used in [33]. Most material parameters, such as elastic constants and reference yield stress, are representative of aluminum alloys. The initial density, however, is taken to be greater than that for aluminum to increase the stable time increment in the dynamic calculations. Nevertheless, we note that the material density is an important parameter since the inertial resistance to motion, $\tilde{H}^{-1} \propto \sqrt{\rho_0}$ (see the parameter $\tilde{H}^{-1}$ introduced just after Eq. (3.28)).

Symbol	Property and units	Value
ρ_0	Initial density (kg/m^3), Eq. (2.13)	7600
C_p	Specific heat (J/kgK), Eq. (2.12)	465
G	Elastic shear modulus (GPa), Eq. (2.7)	26.9
K	Bulk modulus (GPa), Eq. (2.7)	58.3
q_1	Material parameter, Eq. (2.1)	1.25
q_2	Material parameter, Eq. (2.1)	1.0
σ_0	Reference yield stress (MPa), Eq. (2.2)	300
n	Strain hardening sensitivity parameter, Eq. (2.2)	0.1
m	Strain rate sensitivity parameter, Eq. (2.2)	0.01
b	Temperature sensitivity parameter, Eq. (2.3)	0.1406
c	Temperature sensitivity parameter (K^{-1}), Eq. (2.3)	0.00793
ε_0	Reference strain, Eq. (2.2)	0.00429
$\dot{\varepsilon}_0$	Reference strain rate (s^{-1}), Eq. (2.2)	1000
T_0	Reference temperature (K), Eq. (2.3)	293
$\langle f_0 \rangle$	Average initial void volume fraction	0.01
f_c	Void volume fraction at which voids coalesce, Eq. (2.10)	0.12
f_f	Void volume fraction at final fracture, Eq. (2.10)	0.25
f_u	Ultimate void volume fraction, Eq. (2.10)	0.8
β	Taylor-Quinney coefficient, Eq. (2.12)	0.9

Table 1. *Parameters used in the finite element calculations and the linear stability analysis.*

3. 1D analytical model

In this section we develop a 1D linear perturbation analysis to model necking instabilities in Gurson-type (porous) metallic bars subjected to dynamic stretching. To the authors' knowledge, this is the first analytical model developed to study dynamic necking instabilities in porous materials. The model includes the effect of inertia and uses the Bridgman's correction factor to account for the multiaxial stress state that develops inside the necked region.

(a) Governing equations

We consider a cylindrical bar with initial length L_0 and mechanical behavior described by the constitutive framework presented in section 2. The specimen is subjected to constant stretching velocity on both ends and it is assumed that this loading condition is always satisfied. Also the elastic deformations are neglected so that the macroscopic plastic strain equals the macroscopic total strain.

The fundamental equations governing the problem are:

- **Kinematic relations**
  The macroscopic axial true (logarithmic) strain E and strain rate $\dot{E}$ are defined as:

$$E = \ln\left[\left(\frac{\partial x}{\partial X}\right)_t\right]; \qquad \dot{E} = \frac{\partial E}{\partial t} \tag{3.1}$$

  where X is the Lagrangian axial coordinate $\left(-\frac{L_0}{2} \leqslant X \leqslant \frac{L_0}{2}\right)$ and x the Eulerian axial coordinate. These are related as $x = X + \int_0^t v(X,\tau)d\tau$, where the current axial velocity v is related to E and $\dot{E}$ through the continuity equation:

$$\frac{\partial v}{\partial X} = \dot{E}e^E \tag{3.2}$$

  The strain and strain rate in the matrix material, and their relations, were defined in section 2.

- **Momentum balance in the axial direction**

$$\rho A_0 \frac{\partial v}{\partial t} = \frac{\partial\left(A\Sigma^{avg}\right)}{\partial X} \tag{3.3}$$

  where $A_0 = \pi R_0^2$ and $A = \pi R^2$ are the initial and current cross section areas of the bar, and R_0 and R are the initial and current cross section radii, respectively. In Eq. (3.3), Σ^{avg} is the average axial macroscopic stress defined as:

$$\Sigma^{avg} = B(\theta)\,\Sigma \tag{3.4}$$

  where Σ is the uniform axial macroscopic stress and $B(\theta)$ is the correction factor introduced by Bridgman [34] to take into account that, in a necked section, the local axial stress is enhanced by hydrostatic stresses. The correction factor is defined as:

$$B(\theta) = \left(1 + \theta^{-1}\right)\ln(1+\theta) \tag{3.5}$$

  with,

$$\theta = \frac{1}{2}R\left(\frac{\partial^2 R}{\partial x^2}\right) \tag{3.6}$$

  While the Bridgman approximation for necking was developed for elastic-perfectly plastic material response under quasi-static loading conditions, several works [25,35] have demonstrated the capacity of this approach to model the stress state in a necked section for strain rate sensitive materials under dynamic conditions. In particular, Vaz-Romero et al. [35] have recently compared a 1D linear stability analysis of the kind developed here with the 3D approach developed by Mercier and Molinari [19], and a

good agreement between the two models was found. The estimation of stress state inside a necked region by the Bridgman correction in our 1D analytical model precludes the development of short necks, as demonstrated in [17,26]. The comparison between the predictions of the linear stability analysis and the finite element results presented in section 6 of this manuscript further justifies the use of Bridgman correction to describe the multiaxial stress state that develops inside the necked region of a dynamically loaded bar.

The integration of Eq. (2.11) allows to obtain the following relation between the current and the initial cross section areas:

$$\mathrm{A} = \mathrm{A}_0 \left(\frac{1 - f_0}{1 - f} \right) e^{-E} \tag{3.7}$$

with

$$E_{rr} = E_{\theta\theta} = -\frac{1}{2} \ln \left(\frac{\mathrm{A}_0}{\mathrm{A}} \right) \tag{3.8}$$

and

$$\det(\mathbf{F}) = \frac{1 - f_0}{1 - f} \tag{3.9}$$

where E_{rr} and $E_{\theta\theta}$ are the radial and circumferential true macroscopic strains, respectively.

- **Mass conservation**
  Under uniaxial stress conditions, using Eq. (3.9), Eq. (2.13) can be rewritten as:

$$\rho = \rho_0 \left(\frac{1 - f}{1 - f_0} \right) \tag{3.10}$$

- **Conservation of energy**
  Under uniaxial stress conditions Eq. (2.12) can be rewritten as:

$$\rho C_p \frac{\partial T}{\partial t} = \beta \Sigma^{avg} \dot{E} \tag{3.11}$$

- **Flow strength of the matrix material**
  The matrix flow strength according to Eq. (2.2), is rewritten as:

$$\bar{\sigma} = \Psi \left(\bar{\varepsilon}, \dot{\bar{\varepsilon}}, T \right) \tag{3.12}$$

  where, $\bar{\varepsilon}^p$ and $\dot{\bar{\varepsilon}}^p$ are replaced by $\bar{\varepsilon}$ and $\dot{\bar{\varepsilon}}$, respectively.

- **Work-conjugacy relation**
  Under uniaxial stress conditions Eq. (2.8) can be rewritten as:

$$\Sigma^{avg} \dot{E} = (1 - f)\, \bar{\sigma} \dot{\bar{\varepsilon}} \tag{3.13}$$

- **Flow potential**
  Under uniaxial stress conditions Eq. (2.1) can be rewritten as:

$$\Phi\left(\Sigma, \Sigma^{avg}, \bar{\sigma}, f^*\right) = \left(\frac{\Sigma}{\bar{\sigma}}\right)^2 + 2q_1 f^* \cosh\left(\frac{q_2 \Sigma^{avg}}{2\bar{\sigma}}\right) - 1 - \left(q_1 f^*\right)^2 \tag{3.14}$$

Note, for the 1D case we take, $\Sigma_e = \Sigma$, where Σ is the uniform axial macroscopic stress, and $\Sigma^h = \dfrac{\Sigma^{avg}}{3}$, where Σ^{avg} is the average axial macroscopic stress in the neck region as estimated using the Bridgman's correction factor, Eq. (3.5).

- **Flow rule**
  Under uniaxial stress conditions Eq. (2.9) can be rewritten as:

$$\dot{E} = \dot{\lambda} \frac{\partial \Phi}{\partial \Sigma^{avg}} \tag{3.15}$$

where

$$\frac{\partial \Phi}{\partial \Sigma^{avg}} = \frac{1}{B\left(\theta\right)} \frac{2\Sigma}{\bar{\sigma}^2} + q_1 q_2 \frac{f^*}{\bar{\sigma}} \sinh\left(\frac{q_2 \Sigma^{avg}}{2\bar{\sigma}}\right) \tag{3.16}$$

- **Evolution of void volume fraction**
  Using Eq. (2.9), Eq. (2.11) can be rewritten as:

$$\dot{f} = (1 - f)\dot{\lambda} \frac{3 q_1 q_2 f^*}{\bar{\sigma}} \sinh\left(\frac{q_2 \Sigma^{avg}}{2\bar{\sigma}}\right) \tag{3.17}$$

Note that, in order to consider the axial, radial and circumferential strains of the bar, previous expression is derived using the 3D relations presented in section 2.

Considering the domain $[-\mathrm{L}_0/2, \mathrm{L}_0/2]$, the above-mentioned set of equations are to be solved under the following initial and boundary conditions which are formulated in Lagrangian coordinate system:

- **Initial conditions**

$$\begin{aligned} \bar{\sigma}(\mathrm{X}, 0) &= \sigma_0; \qquad \bar{\varepsilon}(\mathrm{X}, 0) = 0; \qquad E(\mathrm{X}, 0) = 0 \\ v(\mathrm{X}, 0) &= \dot{E}_0 \mathrm{X}; \qquad f(\mathrm{X}, 0) = f_0; \qquad T(\mathrm{X}, 0) = T_0 \end{aligned} \tag{3.18}$$

where the constant $\dot{E}_0$ is the initial macroscopic strain rate in the bar. To be noted that the initial values of Σ, $\bar{\dot{\varepsilon}}$ and $\dot{\lambda}$ are obtained by solving Eqs. (3.13), (3.14) and (3.15) with the initial values provided in (3.18). Note also that during the homogeneous deformation, before necking, $B(\theta) = 1$ and therefore $\Sigma^{avg} = \Sigma$.

- **Boundary conditions**

$$v(\mathrm{L}_0/2, \mathrm{t}) = -v(-\mathrm{L}_0/2, \mathrm{t}) = \dot{E}_0 \mathrm{L}_0/2 \tag{3.19}$$

(b) Linear stability analysis

The fundamental time-dependent solution $\mathbb{S}(\mathrm{X}, \mathrm{t})$, at time t, of previous problem is obtained by integration of Eqs. (3.1)-(3.17) satisfying the initial and boundary conditions given by (3.18)-(3.19). The solution at $\mathrm{t} = \mathrm{t}_1$ is:

$$\mathbb{S}_1(\mathrm{X},\mathrm{t}_1) = (v_1, \bar{\varepsilon}_1, \dot{\bar{\varepsilon}}_1, E_1, \dot{E}_1, \bar{\sigma}_1, \Sigma_1, \Sigma_1^{avg}, \theta_1, \mathrm{A}_1, \mathrm{R}_1, \rho_1, T_1, \dot{\lambda}_1, f_1)^T \tag{3.20}$$

Then, a small perturbation $\delta\mathbb{S}$ given by:

$$\delta\mathbb{S}(\mathrm{X},\mathrm{t})_{\mathrm{t}_1} = \delta\mathbb{S}_1 e^{i\xi\mathrm{X}+\eta(\mathrm{t}-\mathrm{t}_1)} \tag{3.21}$$

is superposed on the fundamental solution, where:

$$\delta\mathbb{S}_1 = (\delta v, \delta\bar{\varepsilon}, \delta\dot{\bar{\varepsilon}}, \delta E, \delta\dot{E}, \delta\bar{\sigma}, \delta\Sigma, \delta\Sigma^{avg}, \delta\theta, \delta\mathrm{A}, \delta\mathrm{R}, \delta\rho, \delta T, \delta\dot{\lambda}, \delta f)^T \tag{3.22}$$

is the perturbation amplitude, ξ is the wavenumber and η is the growth rate of the perturbation at time t_1. Here ξ and η are considered time independent (frozen coefficients method).

The perturbed solution is given by:

$$\mathbb{S} = \mathbb{S}_1 + \delta\mathbb{S} \tag{3.23}$$

and the physical solution is the real part of the perturbed solution with $|\delta\mathbb{S}| \ll |\mathbb{S}_1|$. By substituting Eq. (3.23) into the governing equations and keeping only the first-order terms, linearized equations are obtained. In order to scale the problem and bring to light the key variables which control the loading process, we introduce the following nondimensional groups:

$$\begin{gathered}
\hat{v} = \frac{v}{\mathrm{R}_0\dot{E}_1}; \quad \hat{\bar{\varepsilon}} = \bar{\varepsilon}; \quad \hat{\dot{\bar{\varepsilon}}} = \frac{\dot{\bar{\varepsilon}}}{\dot{E}_1}; \quad \hat{E} = E; \quad \hat{\dot{E}} = \frac{\dot{E}}{\dot{E}_1}; \quad \hat{\bar{\sigma}} = \frac{\bar{\sigma}}{\sigma_0}; \quad \hat{\Sigma} = \frac{\Sigma}{\sigma_0}; \\
\hat{\Sigma}^{avg} = \frac{\Sigma^{avg}}{\sigma_0}; \quad \hat{\theta} = \theta; \quad \hat{\mathrm{A}} = \frac{\mathrm{A}}{\mathrm{A}_0}; \quad \hat{\mathrm{R}} = \frac{\mathrm{R}}{\mathrm{R}_0}; \quad \hat{\rho} = \frac{\rho}{\rho_0}; \quad \hat{T} = \frac{T}{T_0} \\
\hat{\dot{\lambda}} = \frac{\dot{\lambda}}{\sigma_0\dot{E}_1}; \quad \hat{f} = f; \quad \Lambda = e^{-E_1}; \quad \hat{\eta} = \frac{\eta}{\dot{E}_1}; \quad \hat{\xi} = R_0\xi
\end{gathered} \tag{3.24}$$

that yield to the following linearized equations.

- **Kinematic relations**
  Linearization of the macroscopic strain rate and the strain rate in the matrix material yield:

$$\delta\hat{\dot{E}} - \hat{\eta}\delta\hat{E} = 0 \tag{3.25}$$

$$\delta\hat{\dot{\bar{\varepsilon}}} - \hat{\eta}\delta\hat{\bar{\varepsilon}} = 0 \tag{3.26}$$

  The continuity equation, Eq. (3.2), leads to:

$$\delta\hat{v} + i\hat{\xi}^{-1}\frac{1}{\Lambda}\delta\hat{E} + i\hat{\xi}^{-1}\frac{1}{\Lambda}\delta\hat{\dot{E}} = 0 \tag{3.27}$$

- **Momentum balance in the axial direction**
  Linearization of Eq. (3.3) yields:

$$\frac{1}{\tilde{H}^2}\hat{\rho}_1\hat{\eta}\delta\hat{v} - i\hat{\xi}\hat{\mathrm{A}}_1\delta\hat{\Sigma}^{avg} - i\hat{\xi}\hat{\Sigma}_1^{avg}\delta\hat{\mathrm{A}} = 0 \tag{3.28}$$

  The dimensionless parameter $\tilde{H}^{-1} = \sqrt{\dfrac{\rho_0\dot{E}_1^2\mathrm{R}_0^2}{\sigma_0}}$ is the inertial resistance to motion [25,27,36] and is the key parameter in the linear stability analysis [25,26]. The linearized average

macroscopic axial stress, the Bridgman's correction factor and the current cross section area, Eqs. (3.4)-(3.6)-(3.7), are as follows:

$$\delta\hat{\Sigma}^{avg} - \delta\hat{\Sigma} - \frac{1}{2}\hat{\Sigma}_1\delta\hat{\theta} = 0 \tag{3.29}$$

$$\delta\hat{\theta} + \frac{1}{2}\hat{\xi}^2\Lambda^2\hat{\mathrm{R}}_1\delta\hat{\mathrm{R}} = 0 \tag{3.30}$$

$$\delta\hat{\mathrm{A}} - \frac{\hat{\mathrm{A}}_1}{1-\hat{f}_1}\delta f + \hat{\mathrm{A}}_1\delta\hat{E} = 0 \tag{3.31}$$

where the current cross section radius is:

$$\delta\hat{\mathrm{R}} - \frac{1}{2\sqrt{\hat{\mathrm{A}}_1}}\delta\hat{\mathrm{A}} = 0 \tag{3.32}$$

- **Mass conservation**
  Linearization of Eq. (3.10) leads to:

$$\delta\hat{\rho} + \frac{1}{1-f_0}\delta\hat{f} = 0 \tag{3.33}$$

- **Conservation of energy**
  Linearization of Eq. (3.11) leads to:

$$\hat{\rho}_1\tilde{c}\hat{\eta}\delta\hat{T} - \beta\hat{\Sigma}_1^{avg}\delta\dot{\hat{E}} - \beta\delta\hat{\Sigma}^{avg} = 0 \tag{3.34}$$

  where $\tilde{c} = \dfrac{C_p\rho_0 T_0}{\sigma_0}$ is the nondimensional specific heat.

- **Flow strength of the matrix material**
  Linearization of Eq. (3.12) leads to:

$$\delta\hat{\bar{\sigma}} - \hat{P}_1\delta\hat{\bar{\varepsilon}} - \hat{P}_2\delta\dot{\hat{\bar{\varepsilon}}} - \hat{P}_3\delta\hat{T} = 0 \tag{3.35}$$

  where $\hat{P}_1 = \dfrac{1}{\sigma_0}\dfrac{\partial\Psi}{\partial\bar{\varepsilon}}\bigg|_{t_1}$, $\hat{P}_2 = \dfrac{\dot{E}_1}{\sigma_0}\dfrac{\partial\Psi}{\partial\dot{\bar{\varepsilon}}}\bigg|_{t_1}$ and $\hat{P}_3 = \dfrac{T_0}{\sigma_0}\dfrac{\partial\Psi}{\partial T}\bigg|_{t_1}$ are the dimensionless strain, strain rate and temperature sensitivities of the matrix material.

- **Work-conjugacy relation**
  Linearization of Eq. (3.13) leads to:

$$\hat{\Sigma}_1^{avg}\delta\dot{\hat{E}} + \delta\hat{\Sigma}^{avg} - \hat{\bar{\sigma}}_1\left(1-\hat{f}_1\right)\delta\dot{\hat{\bar{\varepsilon}}} - \dot{\hat{\bar{\varepsilon}}}_1\left(1-\hat{f}_1\right)\delta\hat{\bar{\sigma}} + \hat{\bar{\sigma}}_1\dot{\hat{\bar{\varepsilon}}}_1\delta\hat{f} = 0 \tag{3.36}$$

- **Flow potential**
  Linearization of Eq. (3.14) leads to:

$$\hat{Q}_1\delta\hat{\Sigma} + \hat{Q}_2\delta\hat{\Sigma}^{avg} + \hat{Q}_3\delta\hat{\bar{\sigma}} + \hat{Q}_4\delta\hat{f} = 0 \tag{3.37}$$

  where $\hat{Q}_1 = \sigma_0\dfrac{\partial\Phi}{\partial\Sigma}\bigg|_{t_1}$, $\hat{Q}_2 = \sigma_0\dfrac{\partial\Phi}{\partial\Sigma^{avg}}\bigg|_{t_1}$, $\hat{Q}_3 = \sigma_0\dfrac{\partial\Phi}{\partial\bar{\sigma}}\bigg|_{t_1}$ and $\hat{Q}_4 = \dfrac{\partial\Phi}{\partial f}\bigg|_{t_1}$ are the dimensionless derivatives of the flow potential with respect to the uniform macroscopic

stress, the average macroscopic stress, the flow strength of the matrix material and the porosity.

- **Flow rule**
  Linearization of Eq. (3.15) leads to:

$$\delta\hat{\dot{E}} - \hat{M}_1\delta\hat{\dot{\lambda}} - \hat{M}_2\delta\hat{\Sigma} - \hat{M}_3\delta\hat{\Sigma}^{avg} - \hat{M}_4\delta\hat{\bar{\sigma}} - \hat{M}_5\delta\hat{f} - \hat{M}_6\delta\hat{\theta} = 0 \tag{3.38}$$

  where $\hat{M}_1 = \sigma_0 \left.\frac{\partial\dot{E}}{\partial\dot{\lambda}}\right|_{t_1}$, $\hat{M}_2 = \frac{\sigma_0}{\dot{E}_1}\left.\frac{\partial\dot{E}}{\partial\Sigma}\right|_{t_1}$, $\hat{M}_3 = \frac{\sigma_0}{\dot{E}_1}\left.\frac{\partial\dot{E}}{\partial\Sigma^{avg}}\right|_{t_1}$, $\hat{M}_4 = \frac{\sigma_0}{\dot{E}_1}\left.\frac{\partial\dot{E}}{\partial\bar{\sigma}}\right|_{t_1}$, $\hat{M}_5 = \frac{1}{\dot{E}_1}\left.\frac{\partial\dot{E}}{\partial f}\right|_{t_1}$ and $\hat{M}_6 = \frac{1}{\dot{E}_1}\left.\frac{\partial\dot{E}}{\partial\theta}\right|_{t_1}$ are the dimensionless derivatives of the macroscopic axial strain rate with respect to the plastic flow proportionality factor, the uniform macroscopic axial stress, the average macroscopic axial stress, the flow strength of the matrix material, the porosity and the temperature.

- **Evolution of void volume fraction**
  Linearization of Eq. (3.17) leads to:

$$\left(\hat{\eta} - \hat{S}_1\right)\delta\hat{f} - \hat{S}_2\delta\hat{\dot{\lambda}} - \hat{S}_3\delta\hat{\Sigma}^{avg} - \hat{S}_4\delta\hat{\bar{\sigma}} = 0 \tag{3.39}$$

  where $\hat{S}_1 = \frac{1}{\dot{E}_1}\left.\frac{\partial\dot{f}}{\partial f}\right|_{t_1}$, $\hat{S}_2 = \sigma_0\left.\frac{\partial\dot{f}}{\partial\dot{\lambda}}\right|_{t_1}$, $\hat{S}_3 = \frac{\sigma_0}{\dot{E}_1}\left.\frac{\partial\dot{f}}{\partial\Sigma^{avg}}\right|_{t_1}$ and $\hat{S}_4 = \frac{\sigma_0}{\dot{E}_1}\left.\frac{\partial\dot{f}}{\partial\bar{\sigma}}\right|_{t_1}$ are the dimensionless derivatives of the porosity rate with respect to the porosity, the plastic flow proportionality factor, the average macroscopic axial stress and the flow strength of the matrix material.

A non-trivial solution for $\delta\mathbb{S}_1$ can only be obtained if the determinant of the system of linear algebraic equations (3.25)-(3.39) is equal to zero. Application of this condition leads to a fourth-degree polynomial in $\hat{\eta}$ with time dependent coefficients that also depend on the dimensionless wavenumber $\hat{\xi}$:

$$B_4(\mathbb{S}_1,\hat{\xi})\hat{\eta}^4 + B_3(\mathbb{S}_1,\hat{\xi})\hat{\eta}^3 + B_2(\mathbb{S}_1,\hat{\xi})\hat{\eta}^2 + B_1(\mathbb{S}_1,\hat{\xi})\hat{\eta} + B_0(\mathbb{S}_1,\hat{\xi}) = 0 \tag{3.40}$$

For the sake of brevity, $B_4(\mathbb{S}_1,\hat{\xi})$, $B_3(\mathbb{S}_1,\hat{\xi})$, $B_2(\mathbb{S}_1,\hat{\xi})$, $B_1(\mathbb{S}_1,\hat{\xi})$ and $B_0(\mathbb{S}_1,\hat{\xi})$ are not shown explicitly. Eq. (3.40) has four roots in $\hat{\eta}$, two real and two complex conjugates. The requisite for unstable growth of $\delta\mathbb{S}_1$ is given by $\mathrm{Re}(\hat{\eta}) > 0$ and hence the root that has the greater positive real part, $\hat{\eta}^+$, is considered for the analysis. Note that the perturbation growth represents the first stage of the necking pattern. The stabilizing effect of inertia and stress multiaxiality on small and large wavenumbers, respectively, promotes the growth of intermediate modes [18–21]. The mode that grows the fastest is referred to as the critical wavenumber $\hat{\xi}_c$, and it is assumed to determine the average distance between the necks in the localization pattern [26,37]. The critical wavenumber evolves with the strain during the post-uniform deformation regime. Zaera et al. [27] have shown that, under dynamic tension, the critical wavenumber increases with the strain in the bar. For dynamic uniaxial tension, the post-uniform regime lies in between the Considère strain, and the strain at which the full localization process is triggered (see section 6). As further discussed in section 6, the critical wavenumber at the strain which determines the end of the post-uniform regime (or prior to full localization) enables us to calculate the average spacing between the necks in the localization pattern [35].

4. 3D finite element model

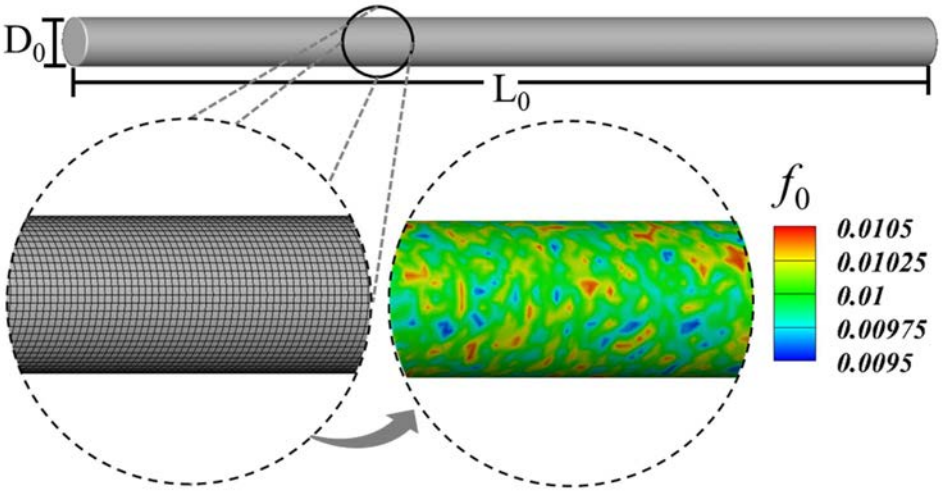

Figure 1. Sketch of the cylindrical bar and zoomed view of the finite element mesh. (Bottom-right) The variation in the initial porosity, f_0, in the zoomed region of the bar. The average porosity in the bar is $f^{avg} = 0.01$ and the amplitude of the perturbation in the initial porosity is $A_{pert} = 5\%$, see Eq. (4.1).

Three dimensional (3D) finite element calculations are carried out to model the response of porous cylindrical bars subjected to initial and boundary conditions given in Eqs. (3.18) and (3.19), respectively. The initial aspect ratio of the cylindrical bars analyzed, Fig. 1, is, $\mathrm{L_0/D_0} = 20$, where $\mathrm{D_0} = 2\mathrm{R_0} = 2\ mm$ is the initial cross section diameter of the bar. The finite element mesh of the cylindrical bar consists of 161,600 twenty node brick elements with initial element dimensions along the axis of the bar being equal to $\mathrm{L_0}/400$. The 3D finite element calculations are based on: the dynamic principle of virtual work using a finite deformation Lagrangian convected coordinate formulation, the constitutive framework detailed in section 2, and the constitutive parameters listed in Table 1. A more detailed description of the finite element formulation and implementation of the same with additional references is given in [33,38–40].

Recall from the introduction that, in the classical statistical theories used to approach the multiple necking problem, distribution of material defects are assumed to be responsible for the distributions of neck sizes in the localization pattern. In the calculations here, the initial porosity or the void volume fraction, f_0, is randomly perturbed in the bar following,

$$f_0 = f^{avg}\left(1 + A_{pert} \times R_{rand}\right) \tag{4.1}$$

where, $f^{avg} = \langle f_0 \rangle$ is the average initial void volume fraction, A_{pert} is the amplitude of the perturbation, and $-1.0 \leq R_{rand} \leq 1.0$ is random number. The value of R_{rand} is generated for each finite element in the bar, thus the porosity in the bar varies at the length scale of the finite element that is more than two orders less than the overall initial length of the bar. The variation in the initial porosity, f_0, in a zoomed region of the bar for one representative case is shown in Fig. 1. The variation of f_0 throughout the bar can be changed by simply generating new set of random numbers for each element for a fixed A_{pert}. Note that seven different distributions of porosity, denoted as Case I, II, ..., VII along the manuscript, for three values of $A_{pert} = 2\%, 5\%$ and 10% have been investigated in this work.

The variation in porosity at such a small length scale i.e. more than two orders less than the overall initial length of the bar is an attempt to describe the characteristic microstructural heterogeneity (inherent distribution of defects) of metallic materials. Following this later in the manuscript, the distribution of porosity will be denoted indistinctly as distribution of defects. Note that, for the initial and boundary conditions, Eqs. (3.18) and (3.19), applied in the finite

element calculations, if the porosity throughout the bar is homogeneous, the specimen stretches uniformly during loading, according to the fundamental solution of the problem, and localization never occurs. This is not the case with commercial finite element codes such as ABAQUS/Explicit that introduce numerical perturbations that are sufficient to break the fundamental solution and trigger localization [26,28,35,41].

5. Key results of the finite element calculations

In this section we present the key results obtained from the finite element calculations. Fig. 2 shows the number of necks, N, incepted in the bar as a function of the macroscopic strain rate, $\dot{E}_0$, imposed on the specimen. For applied macroscopic strain rates $\dot{E}_0 = 1000\ s^{-1}$, $10000\ s^{-1}$ and $50000\ s^{-1}$, results are presented for seven distributions of initial porosity whereas for other values of $\dot{E}_0$ results are presented for a single distribution of initial porosity. For all the cases in Fig. 2, the amplitude of the perturbation in the initial porosity is $A_{pert} = 5\%$, see Eq. (4.1). In the calculations, the formation of a neck is considered when, for a given excursion of strain, the ratio between the peak and the neighboring valleys is ≈ 1.1. The total number of necks in a calculation are determined once the localization pattern is fully developed i.e. further increase in strain does not lead to the formation of new necks. As seen in the figure, the number of necks increases nonlinearly with the applied macroscopic strain rate, featuring a concave-downward shape, as in the experiments and numerical simulations reported for various ductile materials in [25,26,42–44]. The numerical results have been fitted with the power law $\mathrm{N} = 0.455(\dot{E}_0)^{0.365}$.

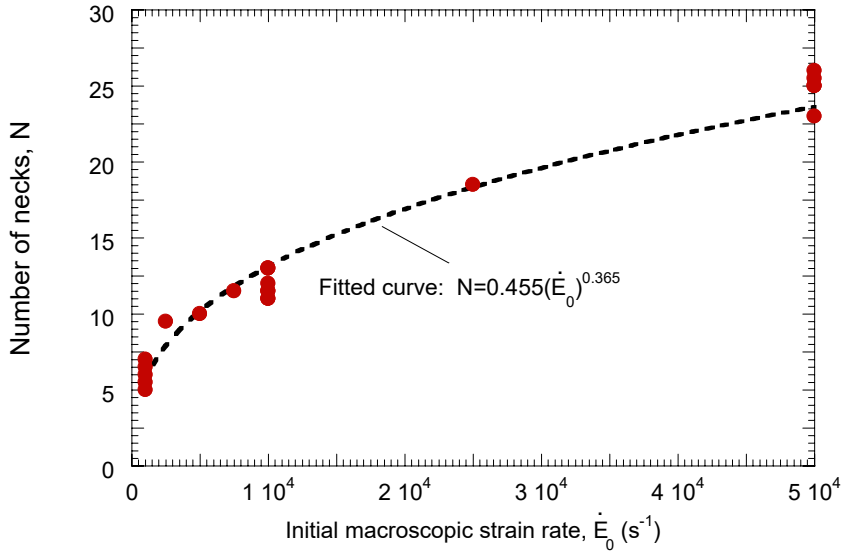

Figure 2. Finite element results. Number of necks N versus applied macroscopic strain rate $\dot{E}_0$. For $\dot{E}_0 = 1000\ s^{-1}$, $10000\ s^{-1}$ and $50000\ s^{-1}$ results are presented for seven distributions of initial porosity whereas for other values of $\dot{E}_0$ results are presented for a single distribution of initial porosity. For all the cases, the amplitude of the perturbation in the initial porosity is $A_{pert} = 5\%$, see Eq. (4.1). The numerical results have been fitted with the curve $\mathrm{N} = 0.455(\dot{E}_0)^{0.365}$.

The influence of the initial porosity distribution on the number of necks is further investigated in Fig. 3 which shows the normalized number of necks $\mathrm{N/N^{avg}}$ for seven distributions of initial porosity (denoted as I, II, ..., VII) for three applied macroscopic strain rates ($1000\ s^{-1}$, $10000\ s^{-1}$ and $50000\ s^{-1}$). Here, $\mathrm{N^{avg}}$ is the average number of necks incepted in the bar considering the seven porosity distributions. For all the porosity distributions, the amplitude of the perturbation

in the initial porosity is $A_{pert} = 5\%$, see Eq. (4.1). As seen in the figure, for $\dot{E}_0 = 1000\ s^{-1}$ there is a variation in the number of necks incepted, for example, N/N^{avg} is 1.2 for the porosity distribution III and 0.85 for the porosity distribution VII. For $\dot{E}_0 = 10000\ s^{-1}$, the variation in the number of necks for the various initial porosity distributions decreases and N/N^{avg} lies within the range $0.9 \leq N/N^{avg} \leq 1.1$ for all seven distributions considered. At even higher loading rate, $\dot{E}_0 = 50000\ s^{-1}$, the maximum variation in the N/N^{avg} is $\approx 5\%$. On one hand, the fact that the number of necks in the bar increases with increasing applied strain rate contributes to decrease in the variation of N/N^{avg} ratio with increasing $\dot{E}_0$. On the other hand, the results in Fig. 3 also suggest that the increase in the applied strain rate reduces the influence of the porosity distribution (i.e. statistical variation in the material defect) on the number of necks that develop in the bar. This can be attributed to the increasing role of inertia at high strain rates as in [26], which promotes the development of some specific wavelengths that play an important role in controlling the neck spacing.

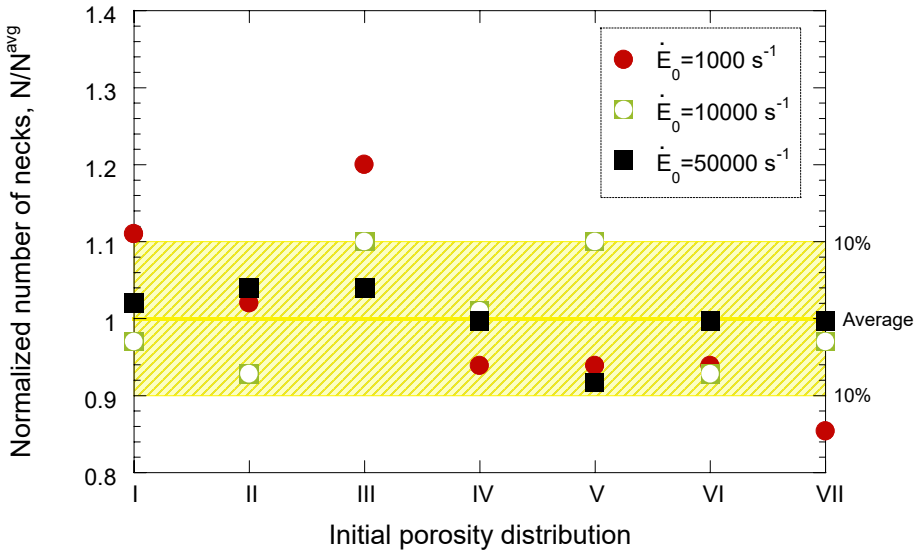

Figure 3. Finite element results. Normalized number of necks N/N^{avg} for three applied macroscopic strain rates $\dot{E}_0 = 1000\ s^{-1}$, $10000\ s^{-1}$ and $50000\ s^{-1}$, and seven distributions of initial porosity. For all the cases, the amplitude of the perturbation in the initial porosity is $A_{pert} = 5\%$, see Eq. (4.1).

Next, histograms of number of necks, N, as a function of the normalized Lagrangian neck spacing, L^{neck}/D_0, for three applied strain rates investigated in Fig. 3 are presented in Fig. 4. The Lagrangian neck spacing, L^{neck}, is the distance between the central sections of two consecutive necks. For all the cases, the amplitude of the perturbation in the initial porosity is $A_{pert} = 5\%$. The results corresponding to seven distributions of initial porosity are included in each histogram and each porosity distribution is plotted with a different color (black, red, dark blue...). As shown in Fig. 4(a), for $\dot{E}_0 = 1000\ s^{-1}$ the distribution of neck spacings is very heterogeneous and the normalized Lagrangian spacing varies in the range $1.9 \leq L^{neck}/D_0 \leq 5.7$, with an average value of 3.4. Hence, the neck spacings for $\dot{E}_0 = 1000\ s^{-1}$ are sensitive to the initial porosity distribution. For instance, for the porosity distribution III (dark blue) the neck spacings vary in the range 1.9 to 3.7, while for the porosity distribution VI (light blue) they vary from 4.2 to 5.5. For $\dot{E}_0 = 10000\ s^{-1}$, Fig. 4(b), the distribution of neck spacings becomes less heterogeneous and the normalized Lagrangian spacings vary from 0.8 to 2.3, with an average value of 1.7. Note that 68% of neck spacings lie within the interval $1.5 \leq L^{neck}/D_0 \leq 2$. For $\dot{E}_0 = 50000\ s^{-1}$, Fig. 4(c), the normalized Lagrangian neck spacings vary in the range 0.4 to 1.1, with an average value of 0.8.

Note that the neck spacings are smaller than those obtained in the simulations presented in [26] for the same strain rate using an ideal incompressible perfectly plastic material model. While the difference is, most likely, due to the plastic compressibility of the material considered in this paper, further research is still needed to clarify this point. Note that for $\dot{E}_0 = 50000\ s^{-1}$, 88% of the neck spacings lie within a narrow interval of $0.75 \leq \mathrm{L^{neck}}/\mathrm{D_0} \leq 1$. Hence the distribution of necks spacings for $\dot{E}_0 = 50000\ s^{-1}$ is *nearly* insensitive to the initial distribution of the porosity considered. In other words, at sufficiently high strain rates, the statistical variation in the material properties or defects seems to have a smaller effect on the multiple necking pattern. The narrowing of the distribution of neck spacing and shifting to smaller lengths with increasing loading rate is in agreement with the experimental observations of Zhang and Ravi-Chandar [12].

The fact that the increase in the applied strain rate reduces the influence of the statistical variation in the material defect on the number and pattern of necks that develop in the bar seems to be reinforced by the results presented in Fig. 5. This graph shows the time evolution of the ratio of the current and the background circumferential logarithmic strain $E_{\theta\theta}/E^b_{\theta\theta}$ along the normalized axial coordinate $\bar{\mathrm{X}} = \mathrm{X}/\mathrm{L_0}$ of the bar for the three applied strain rates investigated in Figs. 3 and 4. The background strain, $E^b_{\theta\theta} = -\frac{1}{2}\ln\left(\frac{\mathrm{A_0}}{\mathrm{A}}\right)$, is the homogeneous strain, Eq. (3.8).

For $\dot{E}_0 = 1000\ s^{-1}$, Fig. 5(a), four different loading times are included in the graph to show the onset and development of the necking pattern in the bar with the initial porosity distribution V. At $\mathrm{t} = 199\ \mu s$, which corresponds to an axial background strain $E \approx 0.18$, Eq. (3.1), the circumferential strain through out the bar is very similar to the fundamental solution. At this point the Considère strain $\left(E^{\text{considère}} = 0.08\right)$ has been exceeded but the fluctuations in the circumferential strain field are almost negligible and cannot be observed in the plot. As further discussed in section 6, and anticipated in section 3, inertia (and material viscosity to a lesser extent) delays flow localization and gives rise to a post-uniform deformation regime in which the bar undergoes quasi-stable deformation. At $\mathrm{t} = 265\ \mu s$, $E \approx 0.23$ which is roughly three times the Considère strain, but only slight fluctuations in the circumferential strain field can be observed. At $\mathrm{t} = 299\ \mu s$, which corresponds to $E \approx 0.26$, the necking pattern becomes apparent. Each excursion of circumferential strain at $\mathrm{t} = 299\ \mu s$ represents a neck. At $\mathrm{t} = 332\ \mu s$, which corresponds to $E \approx 0.28$, the necking pattern is fully developed with heterogeneous spacing between the necks. The width of the excursions of strain, which represents the size of the necks, varies from one neck to another. The height of the excursions, which represents the depth (growth rate) of the necks, also varies from one neck to another.

Similarly for $\dot{E}_0 = 10000\ s^{-1}$, Fig. 5(b), four different loading times are considered to illustrate the inception and development of the necking pattern. Here the initial porosity distribution IV is considered. At $\mathrm{t} = 53\ \mu s$ and $\mathrm{t} = 60\ \mu s$, background axial strains are ≈ 0.43 and ≈ 0.47, respectively, and the strain field in the bar exhibits a wavy profile with peaks as precursors for the necks that develop at larger strains. At $\mathrm{t} = 66\ \mu s$ and $\mathrm{t} = 73\ \mu s$, corresponding background axial strains are ≈ 0.51 and ≈ 0.55, the necking pattern is quite evident. The pattern is an array of necks, suggesting that there are finite wavelengths that determine the neck spacing. In comparison with the results presented for $\dot{E}_0 = 1000\ s^{-1}$ in Fig. 5(a), the spacing between necks is significantly more homogeneous, as also shown in Fig. 4(b). The height of the strain excursions, which characterizes the depth (growth rate) of the necks, is also more uniform.

For $\dot{E}_0 = 50000\ s^{-1}$, Fig. 5(c), time evolution of $E_{\theta\theta}/E^b_{\theta\theta}$ along $\bar{\mathrm{X}} = \mathrm{X}/\mathrm{L_0}$ is shown at three loading times: $\mathrm{t} = 26\ \mu s$, $\mathrm{t} = 33\ \mu s$ and $\mathrm{t} = 40\ \mu s$. The results correspond to the initial porosity distribution I. At $\mathrm{t} = 26\ \mu s$, $E \approx 0.84$ and the onset of a neck-like instability is apparent. Note that the background axial strain is almost 10 times greater than the Considère strain at this point. At $\mathrm{t} = 33\ \mu s$, $E \approx 0.98$ and the excursions in the circumferential strain profile are clearly identifiable. At $\mathrm{t} = 40\ \mu s$, $E \approx 1.10$, and the necking pattern has fully developed. Note that a couple of wide necks split up into two narrow necks with progressive deformation giving rise to a regular pattern with almost constant spacing between the consecutive necks. It is assumed that the splitting of wider necks is due to the activation of smaller and more unstable wavelengths with progressive straining, this is further discussed in section 6.

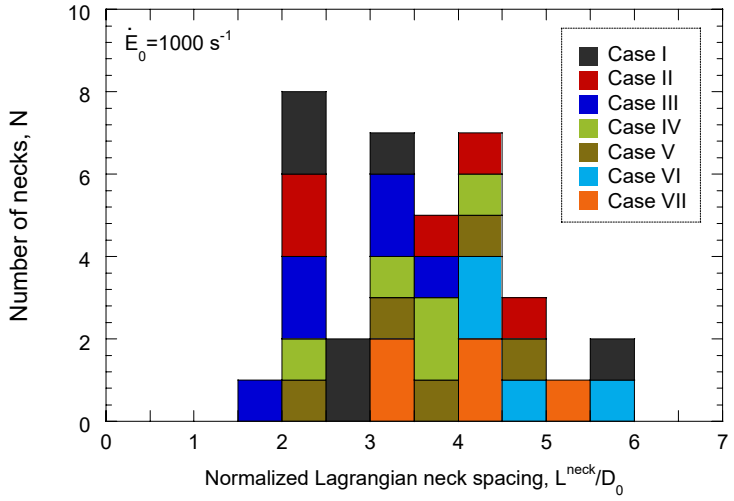

(a)

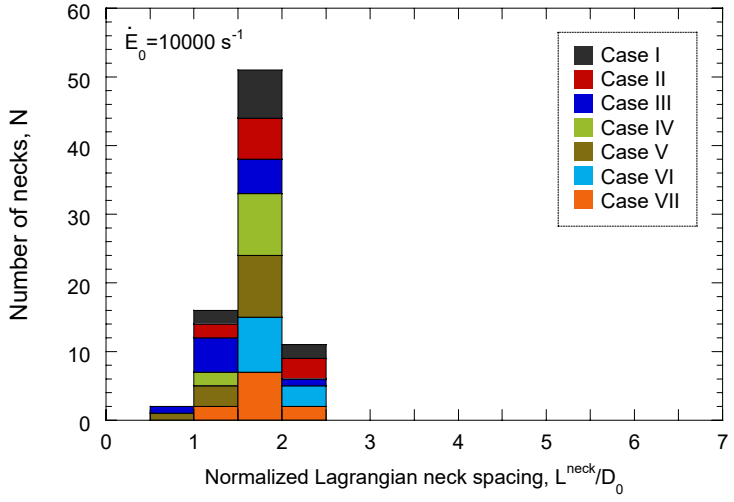

(b)

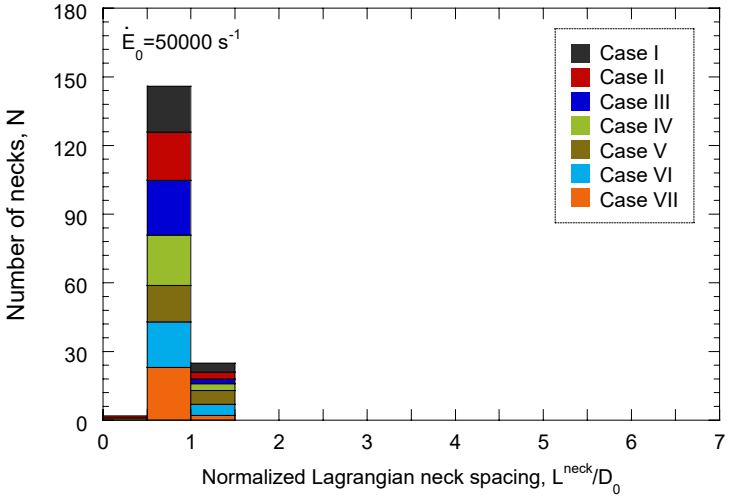

(c)

Figure 4. Finite element results. Histograms showing the number of necks N as a function of the normalized Lagrangian neck spacing L^{neck}/D_0 for three applied macroscopic strain rates: (a) $\dot{E}_0 = 1000\ s^{-1}$, (b) $\dot{E}_0 = 10000\ s^{-1}$ and (c) $\dot{E}_0 = 50000\ s^{-1}$. The results corresponding to seven distributions of initial porosity (seven cases) are included in each histogram. The height of a colored block within a bar of the histogram marks the number of necks with fixed L^{neck}/D_0 for a given case. For all the cases, the amplitude of the perturbation in the initial porosity is $A_{pert} = 5\%$, see Eq. (4.1). For interpretation of the references to color in the text, the reader is referred to the web version of this article.

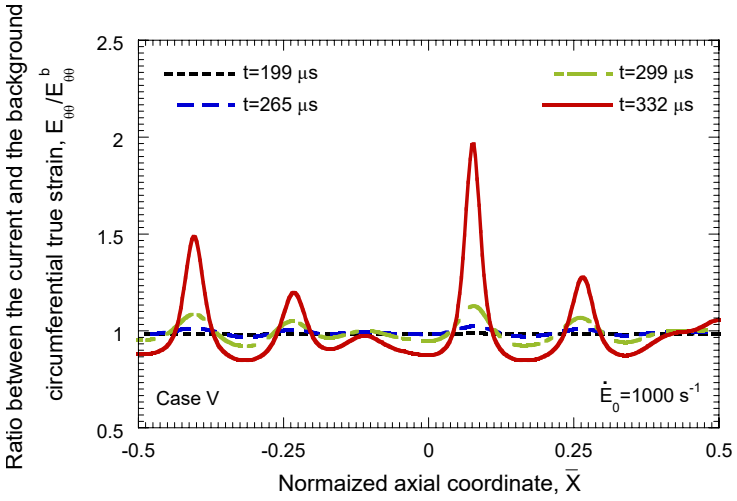

(a)

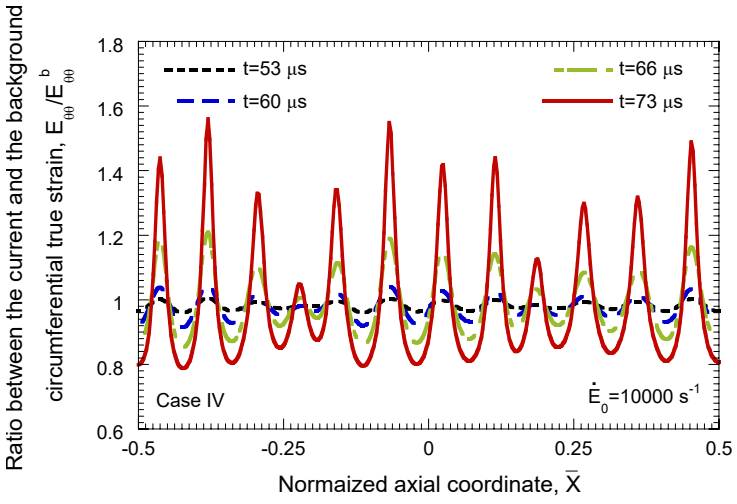

(b)

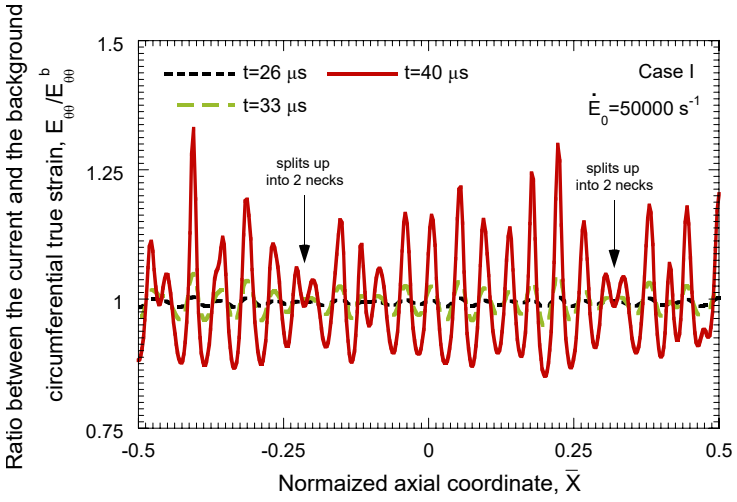

(c)

Figure 5. Finite element results. Time evolution of the ratio of the current and the background circumferential logarithmic strain $E_{\theta\theta}/E^b_{\theta\theta}$ along the normalized axial coordinate $\bar{\mathrm{X}} = \mathrm{X}/\mathrm{L}_0$ for three applied macroscopic strain rates: (a) $\dot{E}_0 = 1000\ s^{-1}$, (b) $\dot{E}_0 = 10000\ s^{-1}$ and (c) $\dot{E}_0 = 50000\ s^{-1}$. For all the cases, the amplitude of the perturbation in the initial porosity is $A_{pert} = 5\%$, see Eq. (4.1).

It is difficult, if not impossible, to experimentally obtain two specimens with exactly the same distribution of defects in order to solely capture the effect of the applied strain rate. However, the finite element calculations allows us to do so. Fig. 6 shows the ratio between the current and the background circumferential logarithmic strain $E_{\theta\theta}/E^b_{\theta\theta}$ versus the normalized axial coordinate $\bar{X}$ for two different initial macroscopic strain rates: $\dot{E}_0 = 1000\ s^{-1}$ and $\dot{E}_0 = 10000\ s^{-1}$. The results correspond to two initial distributions of porosity, Case I (Fig. 6(a)) and Case VI (Fig. 6(b)). The loading times considered ($332\ \mu s$ and $66\ \mu s$, respectively) are such that the necking pattern is fully developed. There are several locations in the bar which develop a neck for $\dot{E}_0 = 1000\ s^{-1}$ but they do not develop a neck for $\dot{E}_0 = 10000\ s^{-1}$ and vice versa. The calculations do not reveal the existence of dominant material heterogeneities that predominantly activate localizations irrespective of the applied strain rate, as sometimes suggested by the classical statistical theories of multiple necking and fragmentation. Nevertheless, more efforts can be made to clarify this point.

The finite element calculation results presented in this section show that the influence of the statistical distribution of material defects (distribution of initial porosity) on the inception and development of necking pattern depends on the applied strain rate. As the strain rate increases, the necking pattern becomes more regular, and seems to be (more) controlled by the development of some specific wavelengths that define the distance between consecutive necks. Further substantiation of this conclusion is pursued in section 6 of the paper. Note, that same conclusions were drawn with the amplitude of the perturbation, see Eq. (4.1), in the initial porosity, $A_{pert} = 2\%$ or 10%, instead of 5% (results for which are presented in this paper). The only difference between the results obtained using $A_{pert} = 5\%$ versus 2% or 10% is that, as the percentage of variation increases (decreases), localization is triggered earlier (later).

6. Comparison between linear stability analysis and finite element results

The axial force F versus the macroscopic true strain averaged over the entire specimen E^{avg}, for the three strain rates considered in Figs. 3, 4 and 5, and three initial porosity distributions are compared with the fundamental solution, Eq. (3.20), in Fig. 7. The amplitude of the perturbation in the initial porosity for the finite element calculations is $A_{pert} = 5\%$. As seen in Fig. 7, for all the applied strain rates, the force obtained from the finite element calculations compares well with the fundamental solution until the end of the post-critical regime. This suggests that the unloading waves emanating from the necks only influence the axial force after the post-critical regime (full localization). The noticeable oscillations in the axial force obtained from the finite element calculations in Figs. 7(b) and 7(c) around the maximum force are primarily due to the fact that the initial values of the field variables, Eq. (3.18), are not the exact fundamental solution of the problem. Therefore, the imposed velocity boundary condition generate stress waves resulting in the oscillations in the axial force. Nevertheless, these oscillations do not affect the onset of the full localization because in our finite element calculations necking does not occur in the absence of heterogeneous distribution of the initial porosity, section 4. Also the oscillations vanish within the post critical regime as seen in Fig. 7. The extent of the post-critical regime is strongly dependent on the applied strain rate but is unaffected by the initial distribution of the porosity. For $\dot{E}_0 = 1000\ s^{-1}$ the post-critical regime ranges from the Considère strain (strain at maximum force) to the macroscopic strain level, $E \approx 0.26$, at which the force decreases rapidly. For $\dot{E}_0 = 10000\ s^{-1}$ and $\dot{E}_0 = 50000\ s^{-1}$ the extent of the post-critical deformation regime is significantly greater, ≈ 0.39 (Fig. 7(b)) and ≈ 0.90 (Fig. 7(c)), respectively. The current and the background strains are virtually coincident in all sections of the bar during the post critical regime (see Fig. 5) because full localization has not occurred yet.

Next, we compare the localization strain and average neck spacing obtained from the finite element calculations and the predictions of the linear stability analysis. To this end, following

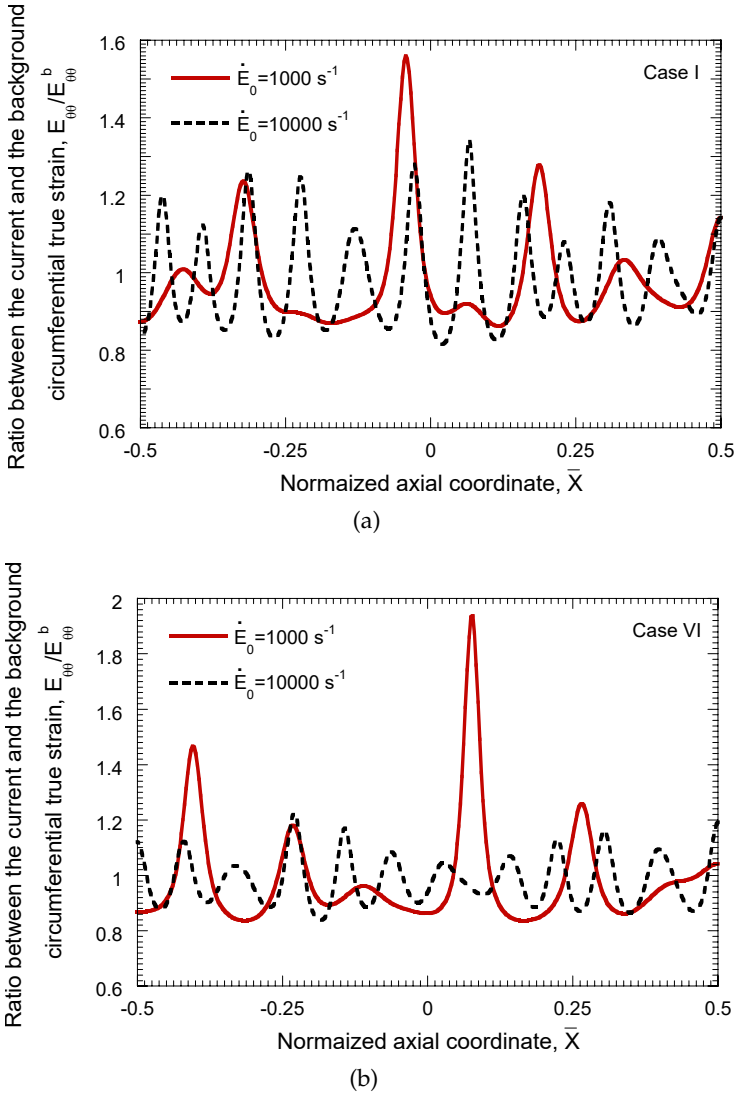

Figure 6. Finite element results. Variation in the ratio of the current and the background circumferential logarithmic strain $E_{\theta\theta}/E^{b}_{\theta\theta}$ along the normalized axial coordinate $\bar{X} = X/L_0$ for two applied macroscopic strain rates: $\dot{E}_0 = 1000\ s^{-1}$ at the loading time $t = 332\ \mu s$, and $\dot{E}_0 = 10000\ s^{-1}$ at the loading time $t = 66\ \mu s$. Two initial distributions of porosity (a) Case I and (b) Case VI are considered. For all the cases, the amplitude of the perturbation in the initial porosity is $A_{pert} = 5\%$, see Eq. (4.1).

[18,22,45], we introduce the concept of cumulative instability index defined as $I = \int_{t^{considère}}^{t} \eta^{+} dt$, where $t^{considère}$ corresponds to the time at maximum force (onset of post-critical regime). Unlike the instantaneous perturbation growth $\hat{\eta}^{+}$, the cumulative index – which integrates the dimensional growth rate of the perturbation– tracks the history of the growth rate of all the growing modes during the post-critical deformation process and, as such, provides a more accurate description of the dominant necking modes which determine the localization pattern for each level of strain [22,35]. The reader is referred to the paper of Vaz-Romero et al. [35] to see a comparison between the results obtained with the instantaneous perturbation growth and the cumulative instability index for the problem of a nonlinear elastic bar subjected to dynamic stretching. The key point is the calibration of the cumulative index in such a manner that the

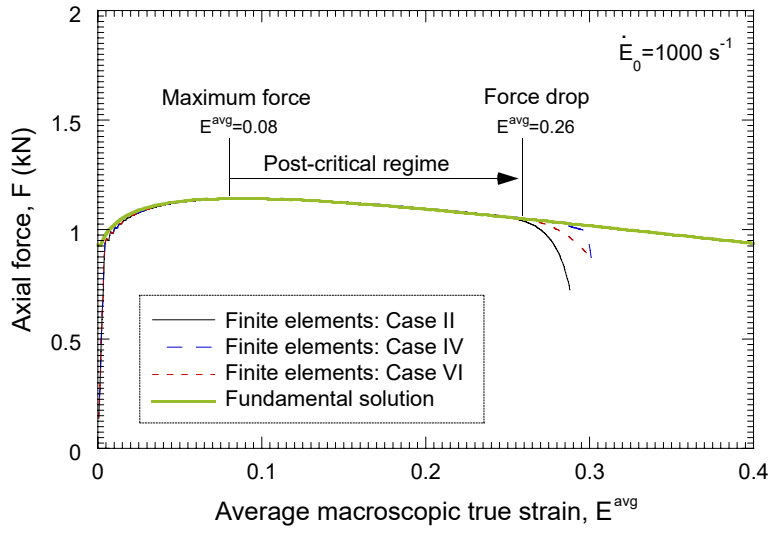

(a)

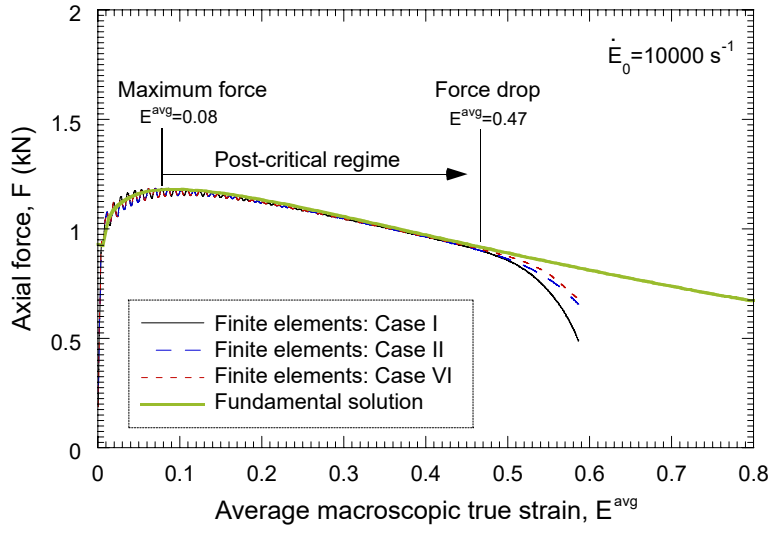

(b)

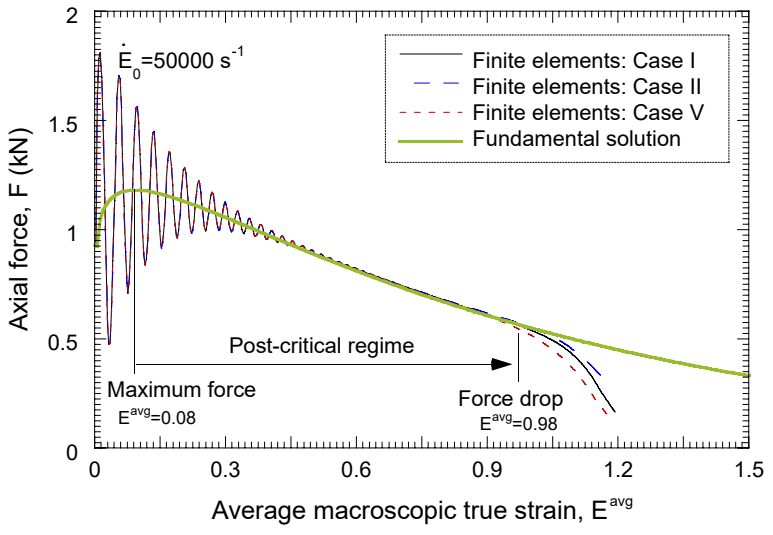

(c)

Figure 7. Finite element results. Axial force F versus average macroscopic true strain E^{avg} for three applied macroscopic strain rates: (a) $\dot{E}_0 = 1000\ s^{-1}$, (b) $\dot{E}_0 = 10000\ s^{-1}$ and (c) $\dot{E}_0 = 50000\ s^{-1}$. For each applied strain rate, finite element results are shown for three initial distribution of porosity. The amplitude of the perturbation in the initial porosity is $A_{pert} = 5\%$, see Eq. (4.1). The fundamental solution given by Eq. (3.20) is represented by the solid lines.

predictive capabilities of the stability analysis can be exploited. For this we rely on the finite element calculations corresponding to the lowest strain rate investigated $\dot{E}_0 = 1000\ s^{-1}$. Recall that the linear stability analysis is only valid to describe the first stages of the necking pattern development (as anticipated in section 3). In other words, it is only valid when the neck-like deformation field shows only a small deviation from the background strain (see Fig. 5). In that case the force exerted on the bar is close to the fundamental solution (see Fig. 7). The calculation for $\dot{E}_0 = 1000\ s^{-1}$ predicts that the drop of the force, i.e. the end of the post-critical regime and thus the upper bound of strain at which the stability analysis can be applied, occurs at $t = 299\ \mu s$ (which corresponds to macroscopic axial strain $E = 0.26$). Inserting this value in the upper limit of the integral which defines the cumulative index we obtain I as a function of the normalized Lagrangian necking wavelength L^{neck}/D_0, calculated as $L^{neck}/D_0 = \pi/\hat{\xi}$ (see [26]).

The $I - L^{neck}/D_0$ curve for $E = 0.26$ is shown in Fig. 8(a). Short wavelengths are damped due to stress multiaxiality effects and long wavelengths due to inertia, such that the curve $I - L^{neck}/D_0$ shows a maximum for a given necking wavelength, called the critical necking wavelength, denoted as $\left(L^{neck}/D_0\right)^c$. The corresponding value of the cumulative index, called the critical cumulative index, is denoted as I^c. For $\dot{E}_0 = 1000\ s^{-1}$ we have that $\left(L^{neck}/D_0\right)^c = 3.89$ and $I^c = 6.72$. The critical wavelength determines the necking mode that grows the fastest and defines the average neck spacing in the localization pattern. Next, we consider cases with applied macroscopic strain rates varying from $2500\ s^{-1}$ to $50000\ s^{-1}$. This range of strain rates corresponds to values of the inertia parameter within the range $0.0126 \leqslant \tilde{H}^{-1} \leqslant 0.251$. For each strain rate, the critical wavenumber and the strain for which the maximum of the $I - L^{neck}/D_0$ curve meets the condition $I = I^c$, are determined. This process is exemplified in Figs. 8(b) and 8(c) which show the cumulative instability index I versus the normalized Lagrangian wavelength L^{neck}/D_0 for $\dot{E}_0 = 10000\ s^{-1}$ and $\dot{E}_0 = 50000\ s^{-1}$. The greater the strain rate, the greater the strain required to meet the criterion $I = I^c$. Note that the increase in the applied strain rate has a strong damping effect on long wavelengths due to the increase in inertial effects and the maximum of the $I - L^{neck}/D_0$ curve moves to shorter wavelengths. Using a critical value for the cumulative index is based on the idea that there exists a certain level of material instability that triggers the localization process. We acknowledge that this is a rather crude idea but it allows us to calibrate the linear stability analysis in a simple manner, and check its predictive capabilities.

The comparison between the localization strains obtained from the finite element calculations –corresponding to the drop in the force– and the predictions of the linear stability analysis –strain at which the criterion $I^c = 6.72$ is fulfilled– is shown in Fig. 9(a). Good agreement between the finite element results and the analytical predictions is noted. The maximum difference between finite element predictions and analytical predictions is within 15%. As shown in the figure, the localization strain increases nonlinearly with the parameter $\tilde{H}^{-1}$ due to the stabilizing effect of inertia on the material flow stress. In these plots we use the inertia parameter, $\tilde{H}^{-1}$, instead of the strain rate, $\dot{E}_0$, in order to better compare our results with the numerical and experimental data available in the literature for different materials (or constitutive model/parameters) and specimens. The variation of localization strain with the parameter $\tilde{H}^{-1}$ for porous aluminum and copper bars obtained from the finite element calculations of Guduru and Freund [28] are also shown in Fig. 9(a). Despite the differences in the constitutive model parameters used, and the fact that the numerical perturbations triggered localization in the calculations of [28], a good qualitative agreement between their and our results is noted from Fig. 9(a). The comparison between the average neck spacing obtained from the finite element calculations and the critical wavelength predicted by the linear stability analysis –necking wavelength for which the criterion $I^c = 6.72$ is fulfilled– is shown in Fig. 9(b). The agreement between the numerical predictions and the analytical predictions is excellent. It shows that the linear stability analysis, calibrated using a reference value for the cumulative index, can be used to predict the average necks spacing in the bar for a wide range of values of $\tilde{H}^{-1}$ (i.e. a wide range of applied strain rates). This is remarkable, especially taking into account the simplicity of the analytical model which includes a series of hypotheses (waves effects neglected, 1D character, linear nature, frozen perturbation coefficients,

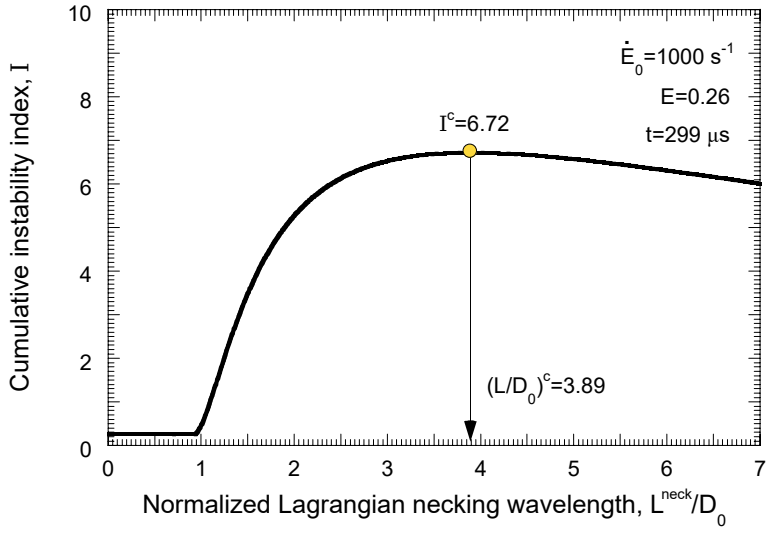

(a)

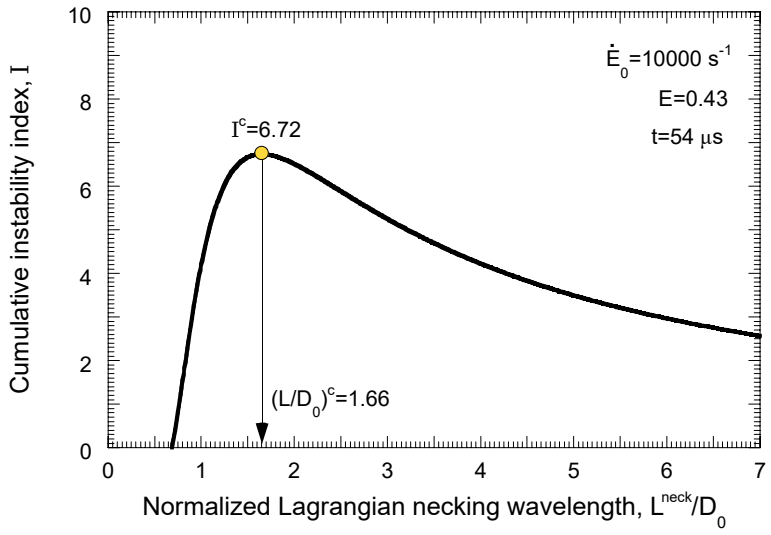

(b)

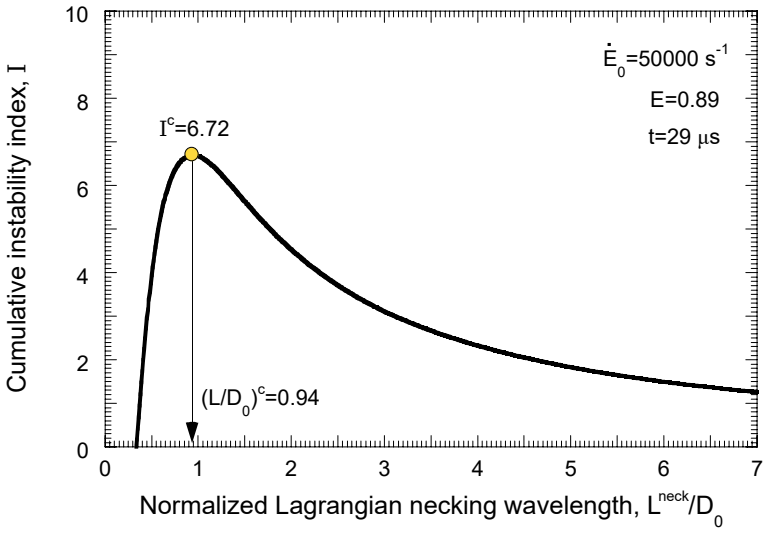

(c)

Figure 8. Linear stability analysis. Cumulative instability index $I = \int_{t^{considère}}^{t} \eta^{+} dt$ versus normalized Lagrangian necking wavelength L^{neck}/D_0 for three applied macroscopic strain rates. (a) $\dot{E}_0 = 1000\ s^{-1}$, $E = 0.26$ and $t = 299\ \mu s$. (b) $\dot{E}_0 = 10000\ s^{-1}$, $E = 0.43$ and $t = 54\ \mu s$. (c) $\dot{E}_0 = 50000\ s^{-1}$, $E = 0.89$ and $t = 29\ \mu s$. The strains considered in each case are such that the maximum of the $I - L^{neck}/D_0$ curve is $I^c = 6.72$.

Bridgman correction...) to make it mathematically tractable. In Fig. 9(b), we also compare the variation of average neck spacing with $\tilde{H}^{-1}$ for aluminum and copper bars obtained from the finite element calculations of Guduru and Freund [28] and experiments of Grady and Benson [46] with our results. A good qualitative agreement between our results and that of Guduru and Freund [28] is noted. In the experiments of [46] only a limited range of values of $\tilde{H}^{-1}$ was covered, nevertheless, the experimental data show a decrease in L^{neck}/D_0 with increasing $\tilde{H}^{-1}$, in line with our results. The quantitative differences in Fig. 9(b) is likely due to the differences in the constitutive model parameters considered here and in [28], and the fact that the constitutive parameters used here were not calibrated to describe the mechanical response of the materials tested in [46].

Furthermore, the linear stability analysis allows us to explain the increasing (decreasing) scatter in the necks sizes obtained from the calculations as the applied strain rate decreases (increases), Fig. 4. Fig. 8 shows that the maximum of the $I - L^{neck}/D_0$ curve becomes weaker (stronger) as the strain rate decreases (increases). In other words, the prevalence of the critical necking wavelength over the other wavelengths is weaker (stronger) as the strain rate decreases (increases). For the lower strain rates considered, the distribution of defects/porosities included in the model can easily favor necking wavelengths different from the critical one that could grow faster, leading to the distribution of neck sizes reported in Fig. 4(a). For the higher strain rates considered, the necking wavelengths close to the dominant one show a clear prevalence over other wavelengths, and the distribution of defects do not seem to promote the development of any necking wavelength which is not near the critical one, as shown in Fig. 4(c). These results show that, as the strain rate increases, the spacing between necks in the localization pattern becomes more deterministic as they are more controlled by the inertial effects than the random distribution of the material defects, (at least) for a given constitutive behavior of the material. Recall that the linear stability results are obtained for strains for which, based on the finite element calculations, the field variables in the bar remain close to the fundamental solution.

7. Summary and conclusions

This paper examines the inception and development of multiple necking patterns in porous metallic bars subjected to dynamic tensile stretching at strain rates varying from $10^3\ s^{-1}$ to $0.5 \cdot 10^5\ s^{-1}$ using finite element calculations and linear stability analysis. In the finite element calculations the initial porosity (representative of material defects) is varied randomly along the bar. The constitutive framework employed in the finite element calculations includes many of the hardening and softening mechanisms that are characteristics of ductile metallic materials, such as, strain hardening, strain rate hardening, thermal softening and damage-induced softening. The linear stability analysis developed here, to the best of our knowledge, is the first of its kind for progressively cavitating elastic-viscoplastic materials. The linear stability analysis also takes into account the effects of inertia and stress multiaxiality. The key findings of this work are as follows:

- For the lower strain rates considered, the numerical results show that the distribution of neck spacings is heterogeneous and is sensitive to the initial distribution of the porosity. In addition, different necks in the bar have markedly different sizes and growth rates. A rational explanation to these results stems from the linear stability analysis which shows that, due to the *limited* contribution of inertia to the loading process, the critical necking wavelength has a weak prevalence over other growing modes. This seems to be exploited by the defect included in the calculations to favor necking wavelengths different from the critical one that could grow faster.

- For the higher strain rates considered, the numerical results show that the distribution of necks spacings is homogeneous and largely independent of the initial distribution of the porosity. In addition, different necks in the bar have similar growth rates and sizes.

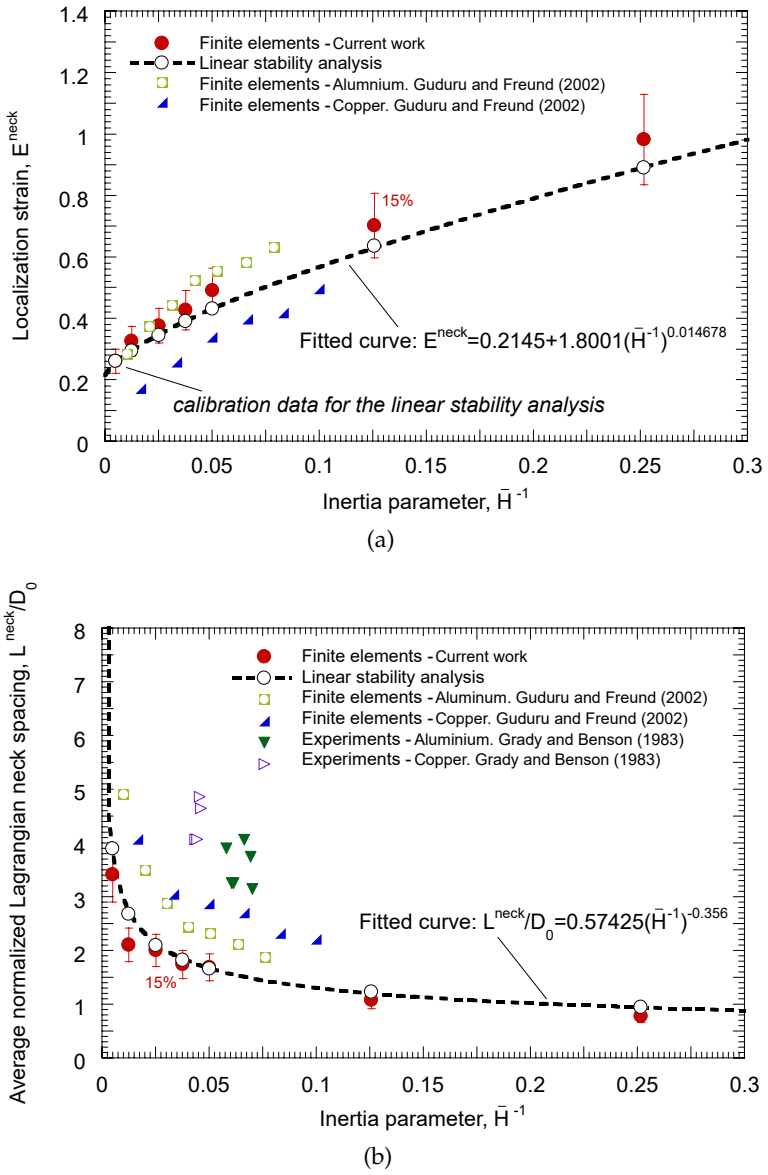

Figure 9. Comparison between finite element calculations performed here (current work), finite element calculations reported in Guduru and Freund [28], experiments reported in Grady and Benson [46] for aluminum and copper, and linear stability analysis. In our finite element calculations the amplitude of the perturbation in the initial porosity is $A_{pert} = 5\%$, see Eq. (4.1). (a) Localization strain E^{neck} versus inertia parameter $\tilde{H}^{-1}$. The linear stability results have been fitted with the curve $E^{neck} = 0.2145 + 1.8001(\tilde{H}^{-1})^{0.014678}$. (b) Average normalized Lagrangian neck spacing L^{neck}/D_0 versus $\tilde{H}^{-1}$. The linear stability results have been fitted with the curve $L^{neck}/D_0 = 0.57425(\tilde{H}^{-1})^{-0.356}$.

The linear stability analysis shows that, at high strain rates, with the increase in inertia effects, the critical necking wavelength has a strong prevalence over the other growing modes. Hence, the heterogeneous distribution of the porosity do not promote necking wavelengths which are not close to the critical one.

- The linear stability analysis, despite several simplifying assumptions, shows remarkable capacity to predict the localization strain and the average neck spacings in the porous

bar for the range of applied strain rates considered. To this end, the calibration of the linear stability analysis using the cumulative instability index is the key, which we carried out using the numerical results for the lowest applied strain rate. The qualitative and quantitative agreement between linear stability analysis and finite element results suggest that the analytical model captures many of the relevant mechanisms that control the emergence of the multiple necking patterns in the specimens.

In summary, the most important message of this paper is that the random distribution of material porosity triggers regular necking patterns at high strain rates. At high strain rates, inertia effects become very important and the necking pattern seems not to be determined by the initial distribution of the porosity. Here we also show that at high applied strain rates, necking is not incepted at the maximum load (or Considère strain) but is followed by an extended post-critical regime due to the stabilizing effects of inertia. The end of the post-critical regime corresponds to full localization and at this point the load decreases rapidly. The extent of the post-critical regime is found to increase with increasing applied strain rate. The extent of the post-critical regime is also affected by the amplitude of the perturbation in the initial porosity. An increase (decrease) in the amplitude of the perturbation results in slight decrease (increase) in the extent of the post-critical regime but does not affect significantly the necking pattern for a given distribution and loading rate. The post-critical regime will most likely be also affected by, the constitutive behavior of the material as suggested for fully dense materials in [19,20,26,47] and micro-inertia effects for porous materials [48–50]. The concerted numerical and analytical tool developed here can now be used for future research needed to analyze the role of individual hardening/softening mechanisms on the inception and development of multiple necking patterns in porous metallic bars subjected to dynamic tensile stretching. In addition, we note that with the advent of new additive manufacturing techniques for metals, it will soon be possible to manufacture specimens with controlled levels of porosity to fully validate our numerical and analytical results.

Acknowledgements. The authors acknowledge the fruitful discussions with Dr. Guadalupe Vadillo (University Carlos III of Madrid), Dr. Alan Needleman (Texas A&M University, College Station), Dr. Alain Molinari (University of Lorraine, Metz), Dr. Sébastien Mercier (University of Lorraine, Metz) and Dr. Krishnaswamy Ravi-Chandar (University of Texas, Austin). The finite element calculations reported on were carried out using high performance research computing resources provided by Texas A&M University (http://www.hprc.tamu.edu).

Authors' Contributions. All authors contributed equally to this work.

Data Accessibility. This paper contains no experimental data. All analytical and computational results are reproducible.

Funding. KEN, SO and JARM acknowledge the support from the European Union's Horizon2020 Programme (Excellent Science, Marie-Sklodowska-Curie Actions) under REA grant agreement 675602 (Project OUTCOME). JARM is also thankful to the Ministerio de Economía y Competitividad de España (Project EUIN2015-62556) for the financial support that partly supported this work.

Competing Interests. We declare we have no competing interests.

References

1. N. F. Mott, E. H. Linfoot, A theory of fragmentation (January 1943).
2. N. F. Mott, Fragmentation of H. E. shells: a theoretical formula for the distribution of weights of fragments (March 1943).
3. N. F. Mott, A Theory of the fragmentation of shells and bombs (May 1943).
4. N. F. Mott, Fragmentation of shell casings and the theory of rupture in metals (August 1943).
5. N. F. Mott, A theory of fragmentation. application to wire wound bombs such as the American 20 lb. F. (May 1944).
6. N. F. Mott, J. H. Wilkinson, T. H. Wise, Fragmentation of Service Projectiles (December 1944).
7. N. F. Mott, Fragmentation of shell cases, Proceedings of the Royal Society A189 (1947) 300–308.

8. D. Grady, Fragmentation of rings and shells the legacy of N. F. Mott, 1st Edition, Springer-Verlag Berlin Heidelberg, 2006.
9. D. E. Grady, M. E. Kipp, D. A. Benson, Energy and statistical effects in the dynamic fragmentation of metal rings, in: J. Harding (Ed.), Mechanical properties at high strain rates, , Institute of Physics, Bristol, 1984, pp. 315–320.
10. M. E. Kipp, D. E. Grady, Dynamic fracture growth and interaction in one dimension, Journal of the Mechanics and Physics of Solids 33 (1985) 399–415.
11. D. Grady, Fragmentation of expanding cylinders and the statistical theory of N. F. Mott, in: M. D. Furnish, N. N. Thadhani, Y. Horie (Eds.), Shock Compression of Condensed Matter - 2001), , American Institute of Physics, 2002, pp. 799–802.
12. H. Zhang, K. Ravi-Chandar, On the dynamics of necking and fragmentation - I. Real-time and post-mortem observations in Al 6061-O, International Journal of Fracture 142 (2006) 183–217.
13. H. Zhang, K. Ravi-Chandar, On the dynamics of necking and fragmentation - II. Effect of material properties geometrical constraints and absolute size, International Journal of Fracture 150 (2008) 3–36.
14. H. Zhang, K. Ravi-Chandar, On the dynamics of localization and fragmentation-IV. Expansion of Al 6061-O tubes, International Journal of Fracture 163 (2010) 41–65.
15. K. Ravi-Chandar, N. Triantafyllidis, Dynamic stability of a bar under high loading rate: Response to local perturbations, International Journal of Solids and Structures 58 (2015) 301–308.
16. J. L. Dequiedt, Statistics of dynamic fragmentation for a necking instability, International Journal of Solids and Structures 32-44 (2015) 107–120.
17. C. Fressengeas, A. Molinari, Inertia and thermal effects on the localization of plastic flow, Acta Metallurgica 33 (1985) 387–396.
18. C. Fressengeas, A. Molinari, Fragmentation of rapidly stretching sheets, European Journal of Mechanics A/Solids 13 (1994) 251–268.
19. S. Mercier, A. Molinari, Predictions of bifurcations and instabilities during dynamic extensions, International Journal of Solids and Structures 40 (2003) 1995–2016.
20. S. Mercier, A. Molinari, Analysis of multiple necking in rings under rapid radial expansion, International Journal of Impact Engineering 30 (2004) 403–419.
21. S. Mercier, N. Granier, A. Molinari, F. Llorca, F. Buy, Multiple necking during the dynamic expansion of hemispherical metallic shells, from experiments to modelling, Journal of the Mechanics and Physics of Solids 58 (2010) 955–982.
22. S. El Maï, S. Mercier, J. Petit, A. Molinari, An extension of the linear stability analysis for the prediction of multiple necking during dynamic extension of round bar, International Journal of Solids and Structures 51 (2014) 3491–3507.
23. N. J. Sørensen, L. B. Freund, Dynamic bifurcation during high-rate planar extension of a thin rectangular block, European Journal of Mechanics A/Solids 17 (1998) 709–724.
24. V. B. Shenoy, L. B. Freund, Necking bifurcations during high strain rate extension, Journal of the Mechanics and Physics of Solids 47 (1999) 2209–2233.
25. F. Zhou, J. F. Molinari, K. T. Ramesh, An elasto-visco-plastic analysis of ductile expanding ring, International Journal of Impact Engineering 33 (2006) 880–891.
26. J. A. Rodríguez-Martínez, G. Vadillo, J. Fernández-Sáez, A. Molinari, Identification of the critical wavelength responsible for the fragmentation of ductile rings expanding at very high strain rates, Journal of the Mechanics and Physics of Solids 61 (2013) 1357–1376.
27. R. Zaera, J. A. Rodríguez-Martínez, G. Vadillo, J. Fernández-Sáez, Dynamic necking in materials with strain induced martensitic transformation, Journal of the Mechanics and Physics of Solids 64 (2014) 316–337.
28. P. R. Guduru, L. B. Freund, The dynamics of multiple neck formation and fragmentation in high rate extension of ductile materials, International Journal of Solids and Structures 39 (2002) 5615–5632.
29. A. L. Gurson, Plastic flow and fracture behavior of ductile materials, incorporating void nucleation, growth, and interaction, Ph.D. thesis, Brown University Providence, RI (1975).
30. V. Tvergaard, Influence of voids on shear band instabilities under plane strain conditions, International Journal of Fracture 17 (4) (1981) 389–407.
31. V. Tvergaard, On localization in ductile materials containing spherical voids, International Journal of Fracture 18 (4) (1982) 237–252.
32. V. Tvergaard, A. Needleman, Analysis of the cup-cone fracture in a round tensile bar, Acta Metallurgica 32 (1984) 157–169.

33. A. Srivastava, L. Ponson, S. Osovski, E. Bouchaud, V. Tvergaard, A. Needleman, Effect of inclusion density on ductile fracture toughness and roughness, Journal of the Mechanics and Physics of Solids 63 (2014) 62–79.
34. P. W. Bridgman, Studies in large plastic flow and fracture, with special emphasis on the effects of hydrostatic pressure, vol.1, McGraw-Hill Book Company, Inc., New York, 1952.
35. A. Vaz-Romero, J. A. Rodríguez-Martínez, S. Mercier, A. Molinari, Multiple necking pattern in nonlinear elastic bars subjected to dynamic stretching: The role of defects and inertia, International Journal of Solids and Structures 125 (2017) 232–243.
36. P. Knoche, A. Needleman, The effect of size on the ductility of dynamically loaded tensile bars, European Journal of Mechanics A/Solids 12 (1993) 585–601.
37. J. A. Rodríguez-Martínez, A. Molinari, R. Zaera, G. Vadillo, J. Fernández-Sáez, The critical neck spacing in ductile plates subjected to dynamic biaxial loading: On the interplay between loading path and inertia effects, International Journal of Solids and Structures 108 (2017) 74–84.
38. S. Osovski, A. Srivastava, L. Ponson, E. Bouchaud, V. Tvergaard, K. Ravi-Chandar, A. Needleman, The effect of loading rate on ductile fracture toughness and fracture surface roughness, Journal of the Mechanics and Physics of Solids 76 (2015) 20–46.
39. S. Osovski, A. Srivastava, J. Williams, A. Needleman, Grain boundary crack growth in metastable titanium β alloys, Acta Materialia 82 (2015) 167–178.
40. A. Srivastava, S. Osovski, A. Needleman, Engineering the crack path by controlling the microstructure, Journal of the Mechanics and Physics of Solids 100 (2017) 1–20.
41. A. Rusinek, R. Zaera, Finite element simulation of steel ring fragmentation under radial expansion, International Journal of Impact Engineering 34 (2007) 799–822.
42. D. E. Grady, M. E. Kipp, Mechanisms of dynamic fragmentation: factors governing fragment size, Mechanics of Materials 4 (1985) 311–320.
43. M. Altynova, X. Hu, G. S. Daehn, Increased ductility in high velocity electromagnetic ring expansion, Metall Trans A 27 (1996) 1837–1844.
44. D. E. Grady, M. L. Olsen, A statistics and energy based theory of dynamic fragmentation, International Journal of Impact Engineering 29 (2003) 293–306.
45. J. Petit, V. Jeanclaude, C. Fressengeas, Breakup of copper shaped-charge jets: Experiments, numerical simulations, and analytical modeling, Journal of Applied Physics 98 (2005) 123521.
46. D. E. Grady, D. A. Benson, Fragmentation of metal rings by electromagnetic loading, Experimental Mechanics 12 (1983) 393–400.
47. N. J. Sørensen, L. B. Freund, Unstable neck formation in a ductile ring subjected to impulsive radial loading, International Journal of Solids and Structures 37 (2000) 2265–2283.
48. A. Molinari, S. Mercier, Micromechanical modelling of porous materials under dynamic loading, Journal of the Mechanics and Physics of Solids 49 (2001) 1497–1516.
49. C. Sartori, S. Mercier, N. Jacques, A. Molinari, Constitutive behavior of porous ductile materials accounting for micro-inertia and void shape, Mechanics of Materials 80B (2015) 324–339.
50. N. Jacques, S. Mercier, A. Molinari, A constitutive model for porous solids taking into account microscale inertia and progressive void nucleation, Mechanics of Materials 80B (2015) 311–323.